Geophys. J. Int. (2000) **142,** 000–000

New results on the resistivity structure of Merapi Volcano (Indonesia), derived from 3D restricted inversion of long-offset transient electromagnetic data

Michael Commer[1,2], Stefan L. Helwig[2] Andreas Hördt[3], Carsten Scholl[4], Bülent Tezkan[2]

[1]*Earth Sciences Division, Lawrence Berkeley National Laboratory, Berkeley, California, USA.*

[2]*Institute of Geophysics and Meteorology, University of Cologne, Cologne, Germany.*

[3]*Institute of Geophysics and Extraterrestrial Physics, Technical University of Braunschweig, Braunschweig, Germany.*

[4]*Department of Physics, University of Toronto, Toronto, Ontario, Canada.*

Accepted 1999 November 11. Received 1999 October 6; in original form 1999 August 3

SUMMARY

Three long–offset transient electromagnetic (LOTEM) surveys were carried out at the active volcano Merapi in Central Java (Indonesia) during the years 1998, 2000, and 2001. The measurements focused on the general resistivity structure of the volcanic edifice at depths of 0.5–2 km and the further investigation of a southside anomaly. The measurements were insufficient for a full 3D inversion scheme, which could enable the imaging of finely discretized resistivity distributions. Therefore, a stable, damped least–squares joint–inversion approach is used to optimize 3D models with a limited number of parameters. The models feature the realistic simulation of topography, a layered background structure, and additional coarse 3D blocks representing conductivity anomalies. Twenty–eight LOTEM transients, comprising both horizontal and vertical components of the magnetic induction time derivative, were analyzed. In view of the few unknowns, we were able to achieve reasonable data fits. The inversion results indicate an upwelling conductor below the summit, suggesting hydrothermal activity in the central volcanic complex. A shallow conductor due to a magma-filled chamber, at depths down to 1 km below the summit, suggested by earlier seismic studies, is not indicated by the inversion results. In conjunction with an anomalous-density model, derived from a recent gravity study, our inversion results provide information about the southern geological structure resulting from a major sector collapse during the Middle Merapi period. The density model allows to assess a porosity range and thus an estimated vertical salinity profile to explain the high conductivities on a larger scale, extending beyond the foothills of Merapi.

1 INTRODUCTION

The Indonesian volcano Merapi, in the eastern part of Central Java, is one of the most active volcanoes of the Earth. Shown in Fig. 1, it is located in the subduction zone between the Eurasian and Indo-Australian plates. Classified as a high-risk volcano, the most recent activity in the year 2006 has again shown the permanent danger to life within Merapi's densely populated surroundings. Over more than 60 years, the frequent activity has been systematically observed in order to improve the understanding of eruption history and complex internal processes. Since 1980, international cooperation has increased, enhancing observation capabilities. Under the leadership of the German Geo-Forschungs-Zentrum Potsdam, and in cooperation with the Volcanological Survey of Indonesia (VSI) and other institutions in Indonesia and Germany, a large interdisciplinary monitoring program was initiated in 1994 (Zschau et al. 1998). Because assessing volcanic activity parameters is an important requirement for improving prediction capabilities, one main project goal was the multidisciplinary investigation of the volcano's edifice structure. Electromagnetic methods were employed because of the typically high resistivity contrasts in volcanoes, caused by resistive host rock, conductive magma reservoirs, and associated hydrothermal systems (Jackson & Keller 1972; Fitterman et al. 1988; Lenat et al. 2001). Measurements with the geoelectric (Friedel et al. 2000), magnetotelluric (MT) (M¨uller & Haak 2004), and long-offset transient electromagnetic (LOTEM) (M¨uller et al. 2002; Commer et al. 2005) method were made with the aim of relating Merapi's resisitivity distribution to important factors such as temperature, porosity, and fractures. Furthermore, combining the resisitivity information with structural information, such as density data, provides further insights into the geological history of the volcano. As a long-term goal, such knowledge may provide the information that would enable scientists to assess optimum locations for potential electromagnetic monitoring sites, in addition to the already existing seismological stations.

LOTEM is an electromagnetic controlled–source method, designed for exploration depths down to several kilometers. Initially developed for hydrocarbon exploration and crustal studies (Strack 1992), the technique has been able to provide conductivity information for depths filling a gap between the shallow geoelectric and large–scale MT measurements. The first large LOTEM

survey was carried out at Merapi in 1998. One major result from the data interpretation was the identification of an extended (10–20 $\Omega \cdot \mathrm{m}$) conductive 1–2 km thick layer at depths of 500–1000 m below the surface (M¨uller et al. 2002). Second, strong 3D effects observed on the lower southern flank could be partly explained by a conductive near–surface structure, related to a possible fluid–filled fracture zone.

In 2000 and 2001, further LOTEM measurements were made at Merapi with the aim of more closely investigating the summit area and the southern flank anomaly. The application of a 3D least–squares inversion scheme to a combined data set, consisting of LOTEM data from all three surveys, allowed us to derive an improved model of the gross resistivity structure, featuring the 3D mountain topography, layered sections, and a fault structure (Commer et al. 2005). In agreement with MT results (M¨uller & Haak 2004), these results showed an extended conductor (over a scale of ≈ 15 km) at depths below 1.5 km, with resistivities below $1\ \Omega \cdot \mathrm{m}$. While our previous studies indicate that hot pore fluids at depth may well contribute to the low observed resistivities, the constant volcanic activity suggests that alteration minerals in a locally confined area below the summit may also play an important role. This is known to produce conductivity anomalies in other geothermal systems (Flóvenz et al. 1985; Fitterman et al. 1988) and has also been a possible explanation for MT data showing a large conductivity anomaly below Central Java (Ritter et al. 1998).

In this paper, we present inversion results that shed more light on geological aspects and the sources of high conductivities observed at Merapi. This was made possible by an improved least-squares inversion approach that enabled inverting for different kinds of model parameters describing a simplified 3D structure. Using this capability, we invert for a layered background model including several additional 3D blocks with independently varying resistivity parameters. The motivation of this inversion approach is to investigate the existence of a voluminous conductor below the summit. Further, we have been able to invert an enlarged joint LOTEM data set, thus providing sufficient resolution for the additional model parameters and more information on the southern flank.

The interpretation of the inversion results shall first aim at providing more information about

two structural aspects, which have been discussed by other authors. These are the southern delineation of a caldera border, resulting from a major south-western sector collapse, and the possible presence and location of a voluminous magma reservoir below the summit. We also further investigate the sources for the generally high conductivities. The low rock densities observed in the Merapi region are further evidence that the conducting layers may well be explained by increased salinities in a porous environment. Therefore, salinity estimates along a vertical profile shall be provided.

2 METHODOLOGY

The Marquardt–Levenberg inversion scheme (Levenberg 1944; Marquardt 1963; Jupp & Vozoff 1975; Huang & Palacky 1991) is employed to refine a coarse 3D model of Merapi. The scheme is a stable iterative method in the presence of ill-posed inversion problems, where small changes in the data can lead to large changes in both the solution and in the process that finds the solution. The principles of the Marquardt–Levenberg method are outlined in Appendix A. In Appendix B, we describe the data transformation used to address the large amplitude range of LOTEM data, as well as a corresponding model parameter transformation.

To compute the predicted data through forward modelling, we employ the finite–difference (FD) code of Druskin & Knizhnerman (1988; 1994), based on the spectral Lanczos decomposition method (SLDM). The code solves the 3D diffusive Maxwell equations using Krylov subspace techniques. It is practically unlimited in terms of model complexity and allows an approximation of real geology by defining areas of constant conductivity in the form of rectangular blocks that do not necessarily conform to the FD grid. This is realized by a material averaging scheme to calculate the underlying effective medium (Moskow et al. 1999) and makes the code appropriate for the implementation of arbitrary model parameters.

Convergence characterisics of SLDM, as described by Druskin & Knizhnerman (1994), must be taken into account when designing an FD discretization. In principle, for a given FD grid and earth model, the stability of SLDM depends on both the latest times to be simulated and the highest conductivity contrasts in a model. Since simulating arbitrary topography requires accounting

for the air layer in the discretization grid, the difficulty lies in the high resistivity contrast between the air and the earth, along with the requirement for a rectilinear FD grid. H¨ordt & M¨uller (2000) carried out extensive studies on the simulation of LOTEM data from mountainous terrain using the SLDM code. Here, following their results, we make sure that a contrast of 100:1 (air:earth) is kept during an inversion, providing stable and realistic results. This has been accomplished by carrying out preliminary test inversions and fixing the air-layer conductivity accordingly. We employ five different FD grids in total for the calculation of the data predictions, to account for different LOTEM transmitters and the large spatial distances between the receiver positions. The grids are adapted in both their size and grid spacing to the different transmitter-receiver configurations and to the measurement time ranges. The difficulty one has with the SLDM scheme in the presence of long time ranges is addressed by using separate FD grids, for early and late simulation times. To ensure stability when the material properties change during the inversion, each grid's response is tested for consistency against varying model contrasts in a preliminary forward modeling study. For more details on the grid verification procedure, the reader is referred to H¨ordt & M¨uller (2000) and Commer (2003).

In contrast to large-scale inversions, where a model is usually discretized into numerous grid cells, our model is described by only as many parameters as is typical for Marquardt inversions. Hence, we construct a 3D model featuring rather unconventional types of model parameterizations. Fig. 2 illustrates how the topography of Merapi is approximated by vertical columns that are more conductive than the resistive air space. The upward extension of each column is derived from a digital elevation model of Merapi (Gerstenecker et al. 1998). The column diameters are varied such that the discretization is fine at the upper flanks, where the steepness of the terrain is large, while at greater distances the model becomes coarser. To model the regular cone shape of the edifice, the column's base areas are square. Based on earlier studies, we assume a layered background model with the layer boundaries conforming to the topography. Comparative model studies indicated that such a dome–shaped structure provides for much better data fits than a horizontally layered background (Commer 2003). The layered model involves two types of parameters. Similar to 1D inversions, they are given by both the thickness and resistivity of each layer. Note, however,

that here the parameters describe a 3D model of curved layers. The upper corner of Fig. 2 exemplifies how a two–layer background is realized in the model construction procedure. Starting from its upper end (at the air–earth interface), each column is sectioned according to the (global) thicknesses as many times as there are layers. Hence, two layers are specified by two resistivity (ϱ_1, ϱ_2) and one thickness (d_1) parameter. Note that the layer parameters thickness and resistivity are global, thus they are equal for each column.

We further employ an additional type of model parameter that specifies single 3D blocks embedded into the background. The SLDM code does not allow overlapping model blocks. Therefore, the columns overlapped by the additional structures are further subdivided and reshaped into smaller parts, such that an empty space, conforming to the new block, is formed. In practice, this process is repeated for each additional block to be included. In principle, the scheme thus allows the creation of arbitrary 3D shapes that can be cast into model unknowns. However, as dictated by the least–squares method, the inversion is constrained by a limited number of model parameters, a maximum number of eight in this work.

3 GEOLOGICAL BACKGROUND

Merapi is a basalt-to-basaltic-andesite volcanic complex with a maximum altitude of 2911 m. Modern studies of the geological evolution started with Van Bemmelen (1949). He introduced the scenario of an eroded older volcanic edifice, which has began to grow during the Pleistocene. This so-called Old Merapi consists of a sequence of basaltic andesite lavas and intercalated pyroclastic deposits, and is overlain by the deposits of a younger volcanic cone (New Merapi) (Newhall et al. 2000). Fig. 3 sketches the major geological features. The growth of the volcano was interrupted several times by violent magmatic to phreatomagmatic eruptions and one or possibly several Mount St. Helens-type edifice collapses in the southwestern section during the so-called Middle Merapi period, 14000–2200 years before present (Camus et al. 2000; Newhall et al. 2000; Gertisser 2001). These events left a horseshoe-shaped morphology of the older volcanic cone and may have sent large debris avalanches down the western slopes. The border of the sector collapses, pointed out by van Bemmelen (1949) as a “hyperbolic fault” (dashed line in Fig. 3), was later re-

lated to an avalanche caldera rim with a wider opening angle than supposed by Van Bemmelen (Camus et al. 2000). Aside from the remnants of the older eruptive stages, much of the area surrounding the volcanic complex is covered by pyroclastic deposits of Holocene age, forming an extensive apron around the volcano (Gertisser & Keller 2003). The material below the volcanic deposits was identified as Cenozoic sediments with low densities, as indicated by gravity measurements (Natori 1978). In a recent gravity data inversion study, a mean density of 2241 $\mathrm{kg/m^3}$ and a porosity range of 10–20 % is estimated for the region of Merapi (Tiede et al. 2005). Earlier, Van Bemmelen (1949) identified the basement sediments as marine tertiary formations and cites an incomplete consolidation of the 'plastic marine strata' as evidence of the volcano-tectonic collapse. Presently, the volcanic activity is characterized by the extrusion of viscous lavas forming domes in the summit area. The collapse of these lava domes due to gravitational instability causes small-volume pyroclastic flows (nuées ardentes) at regular intervals of a few years.

3.1 A priori geophysical information

To characterize the electrical structure, DC resistivity soundings on the upper flanks (Friedel et al. 2000) and large–scale MT and geomagnetic induction vector measurements (M¨uller & Haak 2004) were also carried out at Merapi. These methods and the LOTEM results (M¨uller et al. 2002; Commer et al. 2005) indicated that the resistivity distribution in the uppermost 1 km is related to the succession of the deposits. The DC resistivity soundings are capable of resolving the upper few hundred meters. On the western and southern flank, the soundings show resistivities above 1000 $\Omega \cdot \mathrm{m}$ within the first 200–300 m, which drop rapidly to values below 100 $\Omega \cdot \mathrm{m}$ and 10 $\Omega \cdot \mathrm{m}$, respectively, to a resolved depth of $\approx$ 800 m. Other volcanological resistivity studies, for example at Newberry Volcano (Oregon) (Fitterman et al. 1988) or Piton de la Fournaise (Réeunion Island) (Lenat et al. 2001), also showed that resistivities are usually high at shallow depths. Friedel et al. (2000) suggested that the decrease of the resistivity below 50 $\Omega \cdot \mathrm{m}$ might indicate the contact zone of a hydrothermal system below the summit, rather than a freshwater saturation of the pyroclastic deposits.

All methods identified a generally strong resistivity decrease with depth. While the exploration

depth of the DC soundings is limited to a maximum depth of ≈ 800 m below the surface, the MT data allowed the resolution of structures at maximum depths of ≈ 1800 m below sea level, as shown by the 3D modeling results in Fig. 4. The model is characterized by several layers with a $1\ \Omega \cdot \mathrm{m}$ conducting bottom layer (C) at 0.4–1.8 km, while at larger depths a resistivity increase is indicated by the data (M¨uller & Haak 2004). According to M¨uller & Haak, the intermediate ($10\ \Omega \cdot \mathrm{m}$) conducting layer (B) and the central conductor (D), indicating a rise of layer B, are necessary to explain the magnitudes of induction vectors from sites in altitudes of 1700–2000 m, although a finer structure could not be resolved. In this paper, we show that the LOTEM data provide important additional information for this region of interest, due to the smaller exploration depth focusing on 0.5–2 km below the surface.

The lateral position of the deep west–east striking anomaly on the southern flank (Structure F in Fig. 4) is possibly connected to the conductivity anomalies identified by the LOTEM data in this area (M¨uller et al. 2002; Kalscheuer et al. 2004; Commer et al. 2005). Model studies have already suggested a vertical fault structure at a position depicted by the dashed line in Fig. 4. We will show further evidence for such a structure, which can possibly be related to the boundaries of the edifice collapse during the Middle Merapi period.

The interpretation of the inversion results in this work is greatly improved in terms of ambiguity by including the results of a recent gravity inversion study (Tiede et al. 2005). In this study, a subsurface 3D density model of the Merapi and Merbabu region was derived by inversion of 443 gravity stations. Using a least-squares inversion approach, a mean density of 2241 $\mathrm{kg/m^3}$ and maximal density anomalies between -242 and +264 $\mathrm{kg/m^3}$ were found. The findings further confirm the relatively high rock porosities of the Merapi region, assumed in order to explain the observed high conductivities (M¨uller et al. 2002; M¨uller & Haak 2004; Commer et al. 2005).

4 THE LOTEM DATA

The joint LOTEM data set comprises two different transmitters and 24 receiver stations. The transmitters consisted of long (1–2 km) horizontal electric dipoles (HED), injecting a square wave current into the ground. A Zonge GGT10 transmitter with 10 kVA power generator supplied the input

current, which was injected through steel pipes. The data acquisition was performed using the TEAMEX (R¨uter & Strack 1991) and a SUMMIT system from DMT specially modified for TEM measurements. Both systems are multichannel remote unit systems that are digitally connected to a data-recording-PC. A single raw transient is usually dominated by 50 Hz (and multiples) power–line noise. Therefore, we collected up to several thousand transients at each station to provide for a sufficient signal–to–noise ratio. They were digitally filtered, using techniques described by Hanstein (1996), and selectively stacked. The uncertainties used for weighting each datum are given by the standard deviation of the distribution resulting from the stacking process.

Fig. 5a presents an overview of all stations comprising the joint data set. Stations 1–6 were recorded in 1998, where the measurement at Station 1 was repeated in 2000 with the SUMMIT equipment, enabling longer recording times and thus a larger depth of investigation. The corresponding transmitter HED-1 was a grounded wire 1 km in length and located to the north approximately 4 km from the summit and an elevation of 1500 m above sea level. The summit Station 1b and Stations 20–49, referred to as southern profile in the following, were measured during 2001. These stations were generated by the transmitter HED-2 with 2 km length, and located at 530 m elevation and 12.8 km distance south from the summit. The southern profile, shown in Fig. 5b, contains 18 stations. Here, we keep the station numbering of Kalscheuer et al. (2004) (Stations 20–49).

All inverted transients are the time derivatives of the magnetic induction. For brevity, we will denote the data components by "B_z", "B_x" and "B_y", where the first corresponds to the vertical magnetic field and the others to the horizontal fields parallel and perpendicular to the transmitter line, respectively. Vertical field components are available at all shown receiver positions. In addition, horizontal components from Stations 4–6 are also included in the interpretation. The complete data set thus amounts to a total of 28 LOTEM transients. Horizontal electric fields were also measured. However, we failed to jointly invert electric fields with the magnetic data. The inversions terminated with a misfit approximately one order of magnitude larger than the one produced from inverting magnetic fields only. Field experience has shown that a poor galvanic connection of the sensor electrodes, caused by the dry and rocky ground at most of the stations, may significantly distort elecric fields, which could be observed at some stations. Moreover, recent studies (H¨ordt &

Scholl 2004) have shown that local inhomogeneities close to the receiver or close to the transmitter cause a time-dependent effect on the electric-field transient, while such effects are limited to early times for magnetic field data. Since we do not consider model complexities that would allow local anomalies, we decided to exclude electric field data from the inversions.

Man-made noise, caused by electrical installations of settlements, was significant on the southern flank, in particular at Stations 34–41 and 49. Here we used a technique called VIBROTEM (Helwig et al. 1999, Helwig 2000). The fundamentals of this technique are related to its seismic counterpart, called VIBROSEIS. VIBROTEM can be used to focus the energy of the transmitted signal to a certain frequency band of interest, thus achieving a better signal-to-noise level in the corresponding time-range of the measured transients. Basically, VIBROTEM measurements are impulse responses, in contrast to the step-response of the LOTEM method. For further details on this method, the reader is referred to Appendix C.

5 RESULTS

The data interpretation will be based on two inversion results shown in Figs 6 and 7, referred to as Model A and B, respectively. Both models are characterized by two layered background sections, where the layer boundaries conform to the topography. The vertical section boundary provides the complexity required by the southern anomaly. Model A is based on an earlier inversion result, derived from jointly inverting stations 1–6 (Commer et al. 2005). Here, the additional data of the southern profile allows for greatly increased resolution. Initial model assumptions about the southern section are based on forward modeling results of the southern profile data (Kalscheuer et al. 2004). Inverting the southern profile separately, we found that a minimum of 6 layers gives a good data fit. We further realized that this data (Stations 20–49) cannot be further improved by an inversion where all layer parameters are variable. Hence, the parameters of the southern section were kept fixed, using the findings of the separate inversion, and only the four resistivity and three thickness parameters of the northern part represented the variable part of model A. For the northern section, four layers were found to be appropriate for achieving a good data fit and maximum resolution for most of the parameters.

In the second model (B), we consider an additional complexity. Fig. 7 shows the layered background with three 3D blocks of fixed geometry embedded into the northern section. The resistivity of each block represents an additional unknown. While the southern model part again is not variable, only three layers are now considered for the northern background, to maintain sufficient resolution and limit non-uniqueness. In total, the model contains 8 unknowns. This parameterization was chosen to investigate the possible presence of a magma reservoir, causing a conductivity anomaly with respect to the layered background. Moreover, the presence of magma might also produce a hydrothermal system. Such has been suggested in small depths of a few hundred meters below the summit, because of frequent rainfalls at Merapi and the presence of high contents of meteoric water vapor in the fumarole gases of Merapi (Zimmer et al. 2000). High self-potential observations on the summit were also related to the presence of a convective hydrothermal cell extending close to the present crater (Aubert et al. 2000). Hence, the free resistivity parameters of the blocks aim at investigating whether such a cell shows a resistivity distribution typical for geothermal systems.

Table 1 summarizes the final parameters obtained from the inversions. Also quantified are model resolution results, calculated from a Singular Value Decomposition analysis (Jupp & Vozoff 1975), briefly outlined in Appendix A. Given are each parameter's error bounds, and the corresponding parameter importances for Models A and B. The importances have a range of 0–1, where 1 denotes maximum resolution. (The reader is referred to Kalscheuer et al. (2004) for a detailed resolution analysis of the southern profile). Note that the errors on less important parameters tend to become small because the inversion method only changes such parameters as much as they interact with more important ones. The importances indicate a good resolution for all parameters of Model A. The 28 transients of the combined data set and the corresponding data fits obtained from this model are shown in Fig. 8, where voltages, as used in the inversion, have been converted into early-time apparent resistivities. In view of the limited model complexity, a good data fit is achieved in general. Sign reversals indicating multi–dimensional effects in the vertical fields can be observed at stations 34–40, 5, and 6. The transients of 34–41 and 49 (denoted by vtem) are impulse responses and thus show a first sign reversal from positive to negative voltage. The second

reversals at later times (Stations 34–40), however, indicate a lateral anomaly along the southern profile. A remarkable result is the qualitative fit of these sign changes, showing that the fault plane is an appropriate model assumption.

Further sign changes are observed in the step response vertical fields at Stations 5 and 6. These reversals are caused by the mountain effect (H¨ordt & M¨uller 2000). Similar to a superficial conductive anomaly in a flat underground, the mountain acts as a conductor in the resistive air space between the northern transmitter (HED–1) and the southern flank. This effect is known to be caused by current channeling, where the magnetic field curls around the current concentration in a conductive body (Newman 1989), in this case the more conductive mountain, and the vertical response is antisymmetric on either side of the mountain. Fitting this data shows the importance of including topography in the model.

The shape of the transients produced from Model B is very similar to Model A. Thus, for a comparison we have only annotated both data fitting errors (χ_A for Model A and χ_B for B) in Fig. 8. Larger values for χ_B, particularly at 37, 39, and 06-by, are mainly caused by a worse data fit at times before 10^{-2} s, because the corresponding data weights are usually larger than at later times. Nevertheless, the result B allows us to draw two conclusions. First, the three block parameters reveal a similar resistivity decrease with depth as the layered background. In spite of suffienct resolution, the additional structure given by these blocks appears not significant for a data fit. This may explain the relatively small importance of the second block (67 $\Omega \cdot \mathrm{m}$) as its resistivity hides it within the second layer in the final model. Second, Model B provides for a remarkably better data fit for the late times of the 06-bz transient, as shown in comparison in Fig. 9. Note, however, that the misfit errors remain similar because of slightly larger early–time deviations. This finding demonstrates that a more complex model is required for a fit of this data, while a layered background is a good approximation for the gross resistivity distribution. A shallow conductor, with low resistivities comparable to the bottom layer, at a depth range of the two upper 3D blocks is not indicated. Note that we have also carried out similar inversions with 3D blocks at even smaller depths, yet with no further improved data fit compared to the one produced by Model A.

Another alternative approach involved the same structure as in Model B, yet with only one variable resistivity parameter assigned to the three blocks below the summit.

6 INTERPRETATION

While the station density of the LOTEM data is not sufficient for deriving a finely structured 3D model, our results enable us to draw conclusions about the resistivity distribution and related geological questions on a gross scale outlined by the shown models.

6.1 Southern flank anomaly

The model feature of a west-east striking fault might be a simplification of a more complex transition to a different layering below the southern flank. Its location cuts the west-east striking conductor at a depth of 1.5 km derived from MT data (Fig. 4, F). Further, it coincides with a near-surface west-east striking 3D anomaly derived from another LOTEM profile, causing strong sign reversals on the lower southern flank (M¨uller et al. 2002). However, a joint inversion for the parameterization of model A, including these measurements, could not be accomplished with reasonable data fits. This finding indicates a more complex anomaly, particularly at smaller depths, which might require a larger number of parameters in a model. For a more detailed interpretation of the layered model south of the fault line, the reader shall be referred to the findings of Kalscheuer et al. (2004), who have accomplished 1D inversions with different model smoothing constraints. The Marquardt inversion is known for its high influence of the starting model on the inversion result, a drawback even larger for less resolved model parameters. Although the importances in Table 1 indicate a rather good overall resolution for the layer parameters, it is likely that a variety of other equivalent models can be found for the layered sections north and south of the fault line. Nevertheless, we are interested in a more qualitative interpretation. While both layered sections show a steep conductivity increase with depth, the finer layering in the south might indicate different deposits south of the fault line.

The scenario of a fault might shed some light on the question about the southern border of a large avalanche caldera rim, discussed in detail by Camus et al. (2000) and Newhall et al. (2000).

Such a caldera was interpreted as the remnant of a huge gravitational collapse of the south-western flank during the Middle Merapi period, assumed between 14000–2200 years BP (Camus et al. 2000). In the work of Van Bemmelen (1949), the boundaries were identified as shown by the hyperbolic fault in Fig. 3 (dashed line). The studies of Camus et al. (2000) suggest a wider opening angle of this avalanche caldera rim (solid line). Its southward extension is known as the Kukusan fault. It runs east of Gunung Kendil, which is known to be a remnant of the Middle Merapi period, because of its characteristic lava flows, known as Batulawang series. However, the extension of the crater breach further southward is questionable. Camus et al. (2000) relate its course to the question of whether the Plawangan and Turgo hills are remnants of the sector collapse, similar to Gunung Kendil. In this case, the hills would be megablocks which were shifted from their origin by the edifice collapse. Although the lava flows of Plawangan do not contain strong indicators of displacement, the passing of the border south of the Plawangan-Turgo hills is still considered (Camus et al. 2000).

In the following, we tentatively relate the section border of our inversion results to a proposed southern extension of the avalanche caldera rim. Interpreting gravity measurements, Tiede et al. (2005) found that a west-east striking low-density anomaly coincides with the southern flank conductivity anomaly derived from the LOTEM results. The density model of the Merapi region is shown for several depths in Fig. 10, together with the caldera rim as suggested by Camus et al. (2000) and its southward extension. For the south-western region, the density model indicates some interesting relationships between the density distribution and the geology resulting from the sector collapse. A strong positive density anomaly (Fig. 10, g) coincides with the location of the Gendol Hills, at approximately 20 km west-southwest of Merapi. Camus et al. (2000) interpret these hills as the visible part of the debris-avalanche deposit, because of an observed strong brecciation and alteration. In contrast, Newhall et al. (2000) list several observations suggesting that these hills are erosional remnants of the Old Merapi, protruding from the deposits of the large landslide. The latter scenario has also been proposed by Van Bemmelen (1949). The gravity observations also suggest that the positive density anomaly can be related to the older andesitic lavas of the Gendol Hills, characterized by a higher density than the surrounding deposits. Following this

interpretation, the negative density anomalies in the south-west might be caused by the younger pyroclastic deposits from the period after the caldera event, although Fig. 10 shows that the large negative density body (a) in the west does not correlate with the northern caldera border. Thus, one might argue that it might be of different origin. Note, however, that the gravity station density north of the caldera border is much lower than south of it. Moreover, the southern part of the density anomaly (a) coincides with the spatially more confined high-conductivity anomaly derived from MT observations (Fig. 4, E).

Based on these observations, we propose that the southern course of the hypothetical caldera rim runs along the negative density anomalies, with values between -100 and -200 $\mathrm{kg/m^3}$ observed at depths of -1 to -4 km (Fig. 10). Starting from the southern end of the Kukusan fault, the fault line passes through the LOTEM profile at 9159.5 km N. Here, as suggested by Tiede et al. (2005), it may be related to the body of negative density anomaly at 438-445 km E and 9157-9160.5 km N. Further south-west, at 430 km E and 9156 km N, the density model shows another small low-density anomaly.

To conclude, assuming that the fault structure of our model originates from the southern branch of the caldera rim, the results would support the theory that the Plawangan-Turgo group are true megablocks of Old Merapi. This would further suggest that the forces caused by the landslide were oriented more towards a south-western direction, while the narrower hyperbolic fault of Van Bemmelen (1949) indicates a more west-southwest direction. The absence of positive density anomalies at the location of the Plawangan-Turgo hills may support the findings of Newhall et al. (2000), who observed differing lithologies between the Gendol Hills and the remnants of Old Merapi, which would include the Plawangan-Turgo group.

6.2 Magma reservoir

The existence of a superficial magma reservoir has been an ongoing controversy. The idea of a conductivity increase caused by such a reservoir is related to the circulation of pore fluids and thus highly conducting hydrothermally altered minerals around a magma body, rather than due to large amounts of melts. For the depth range of 0–500 m, the time delay between the LOTEM transmitter

turnoff and the start times of our data, and the scarcity of summit measurements do not allow to resolve a confined and shallow anomaly.

The inversion result of Model B (Fig. 7) shows that no improved data fit is achieved for Stations 1–6 (Fig. 8). In the presence of a hydrothermally active region at depths of 500–1000 m, and with a size comparable to the additional block parameters, one would expect an anomalously high conductivity for the upper two blocks. It has often been observed that the conductivities in geothermal systems are characterized by high values in a zone above the system, while the actual reservoir can have lower values (Ussher et al. 2000). In such a case we would expect ϱ_{block1} to be smaller than ϱ_{block2}. Despite several inversion attempts with varying starting models, this could however not be observed.

Regarding depths below 1 km, both seismic data (Wassermann et al. 1998) and deformation measurements (Beauducel & Cornet 1999) did not support a magma reservoir. On the other hand, Ratdomopurbo & Poupinet (1995) interpreted a zone with anomalously high attenuation of seismic waves 1.5 km below the summit as a magma chamber. Camus et al. (2000) related both the absence of large ignimbrite eruptions and the quasi-steady magma output to a small superficial reservoir with a capacity of $\approx 1.6 \times 10^7\,\mathrm{m}^3$ (Gauthier & Condomines 1999), rather than a larger deep-seated source. From eruption rates, Siswowidjoyo et al. (1995) estimated a radius of 25 m for the conduit of ascending magma, linking the vent and a possible reservoir. Despite the strong model constraints, the curved-layer background of our models may indicate a rising conductor. The reasonable data fits would thus be further evidence for a central hydrothermal system at a depth of ≈ 1.5 km. This system may be caused by magma-filled pockets or a magma chamber. Model B shows that deeper structural information, characterized by low resistivities, cannot be derived, because the conductive bottom layer remains a dominant feature.

6.3 Alteration processes

The basement conductivities below $1\ \Omega \cdot \mathrm{m}$ in both sections of our models may be related to the local conductivity anomaly below Merapi observed on a regional MT profile across Central Java (Ritter et al. 1998). The MT measurements identified an even larger conductivity anomaly further

inland. Ritter et al. (1998) proposed that geothermal activity, in combination with hydrothermal fluids, are a possible source. According to Camus et al. (2000), most Merapi lavas are calc-alkaline and high-K basaltic andesites. Furthermore, the chemical composition becomes more basaltic towards larger depths. Conductive anomalies in basaltic environments are known to be caused by alteration, where higher temperatures increase the number of ions at clay-water interfaces .

Studying the temperature dependence of Icelandic, water-saturated, basaltic rocks, Flóvenz et al. (1985) have suggested dominating interface conduction caused by alteration minerals as an explanation for resistivities below 10 $\Omega \cdot \mathrm{m}$. Common alteration products, such as smectite, zeolites, and calcite were for example found in boreholes at Newberry Volcano (Oregon), where the lava flows are also characterized by large basaltic volumes (Fitterman et al. 1988). Because of Merapi's constant activity and thus high temperatures below the central edifice, we strongly consider interface conduction mechanisms in a confined central hydrothermal system, indicated by the raising layer of our models, as likely to be dominant over pore water conduction.

6.4 Conductive aqueous solutions

The complex history of eruptions and a varying volcanism over time suggests to also differentiate between conduction mechanisms. While alteration is likely to be dominant for the volcanically active central region, we must also consider increased pore water conduction due to high salinities as conductivity sources, in particular at larger distances from the summit. The existence of saline solutions, that are not strictly confined to the volcanically active region, were also considered as most plausible to explain MT measurements up to 8 km away from Merapi's summit (M¨uller & Haak 2004), revealing basement resistivities of 1 $\Omega \cdot \mathrm{m}$ (Fig. 4).

If ionic conduction in pore fluids dominates, assuming no interface conduction and effectively no matrix conductance, an empirical relationship between bulk resistivity of the rock ϱ, fluid resistivity ϱ_w, and connected porosity ϕ has been widely used (Archie 1942),

$$\varrho = a \varrho_w \phi^{-m}. \tag{1}$$

The constants a and m are related to the lithology of a water-bearing rock. Following M¨uller et al. (2002), we choose $a = 1$ and $m = 2$, as typical for volcanic rocks. In a recent work (Commer et

al. 2005), we have provided a salinity estimate of 10 equivalent weight percent (eq. wt. %) NaCl, with a maximum of 25 eq. wt. % assuming a porosity of 5 %, in order to explain the basement resistivities below 1 $\Omega \cdot \mathrm{m}$. Here, we want to deduce a more differentiated salinity profile, based on the layer resistivites of Model A.

Salinity ranges for each layer are deduced from a parameter range for the bulk resistivity, porosity, and temperature. The results are listed in Table 2 for the northern section. Similar values can be assumed for the southern model section, owing to similar bulk resistivities. Our porosity estimates range from 10–20 %, based on the density model derived by Tiede et al. (2005). Together with the parameter bounds of the layer bulk resistivities in Table 1, one obtains minimum and maximum fluid resistivities ϱ_w for each layer by applying eq. 1.

An increased regional heat flow can be expected for the Merapi region due to the constant volcanic activity. Flóvenz et al. (1985) estimate that the temperature gradient outside volcanic zones varies between 50–150 °C/km. Here, we want to assume a mean temperature gradient of 100 °C/km. Using the layer thicknesses, we thus obtain a temperature range, corresponding to the depths of a layer's boundaries. Then, the pairs ϱ_w^{max}, T^{max} and ϱ_w^{min}, T^{min} allow to obtain an estimated salinity range, using conductivity measurements of NaCl solutions as a function of temperature and concenctration (Keller 1988). For Layers 1 and 2, the maximal salinities of 0.2 and 0.7 eq. wt. % indicate a rather dilute solution. A low degree of salinity is in accordance with isotopic investigations at the summit, showing that fumarolic water is mainly of meteoric origin, with only a small volume of magmatic water (Zimmer et al. 2000). The deeper layers 3 and 4 show increased salinities. While the salinity of seawater (≈ 3.5 eq. wt. %) falls well within the range of layer 3, the estimates of the bottom layer show a much higher concentration.

Van Bemmelen (Van Bemmelen 1949) points out that the young quaternary volcanoes of East Java are built upon a basement of plastic and not yet consolidated marine sediments. We thus also want to consider a different rock lithology for the basement layer, which involves different constans a and m for eq. 1. For weekly cemented rocks, usually Tertiary in age, including sandstone and some limestones, values of $a = 0.88$ and $m = 1.37$ are found to be typical (Keller 1988). As shown in Table 2, this would lead to a salinity estimate of 2–10 eq. wt. %. In this case, the low

basement resistivities may well be explained by the intrusion of seawater. It is not uncommon that saline groundwater can be found as far as 10–20 km inland, as for example observed in the southern lowlands of Iceland (Flóvenz et al. 1985). Although Merapi is more than 50 km inland from the southern coast, the high porosity of the marine sediments may still be a plausible explanation for such a far intrusion of seawater.

7 CONCLUSIONS

The Marquardt scheme employed in this paper has proven to be a valid alternative for inversion problems in which insufficient data exist for a full large–scale approach. A priori information is required to find an appropriate model parameterization, but we have here demonstrated that even with only a few parameters some versatility is provided, because unknowns can be adapted to arbitrary model structures of interest. The low computational needs of this method are another advantage. For example, one inversion iteration for Model B requires, for each of the 8 unknowns, computing the model perturbations for each grid, in addition to the response of the unperturbed model. The inversion involves 5 different FD grids. This amounts to a total of 45 forward calculations with the SLDM code per iteration. We distributed these calculations on 6 nodes of a SUN Fire 6800 computer, requiring an average computation time of 1 hour per iteration.

The transition to a different resistivity structure below the foothills of the southern flank is required for a satisfying data fit and further confirms the presence of a vertically extended conductivity anomaly. Its relation to the border of a large avalanche caldera remains hypothetical, because of the insufficient data covering of the southern flank area. Nevertheless, the joint interpretation of the inversion results with the findings of other geophysical studies shows a reasonable agreement with the geological considerations about the major edifice collapse during the Middle Merapi period.

The inversion results provide valuable information about the sources of the low resistivities observed at Merapi. The reasonable data fits for most of the stations calculated from the layered model with a curved shape is evidence supporting the scenario of an upwelling hydrothermal system at depths below 1 km. Our studies further confirm that large magma-filled regions above

depths of 1 km, as a conductivity source, are unlikely. On a larger scale, outlined by the dimensions of our models, the estimations applying Archie's law support the existence of hot saline fluids as the dominant source of high conductivities below depths of 1 km. High rock porosities suggest that the saline fluids may well originate from intruding seawater.

ACKNOWLEDGMENTS

We gratefully acknowledge funding of the research at Merapi by the German Science Foundation (DFG) (Project No. HO1506/8-1). We also wish to thank the German Alexander-von-Humboldt Foundation for currently supporting Michael Commer through a Feodor-Lynen Research Fellowship. Tilman Hanstein, Olaf Koch, J¨orn Lange, Roland Martin and Roland Blaschek helped during the field survey. The Volcanological Survey of Indonesia (VSI, Bandung) and the Merapi Volcano Oberservatory (MVO/BPPTK, Yogyakarta) staff provided a lot of logistical support in Indonesia. The Institut Teknologi Bandung (ITB) supplied the equipment for the LOTEM transmitter. Vladimir Druskin and Leonid Knizhnerman allowed us to use their finite-difference code.

Appendix A: Marquardt inversion scheme

To briefly outline the principles of the Marquardt method, we start from the normal equation of the Gauss–Newton solution of a weighted least–squares problem (Jupp & Vozoff 1975),

$$\mathbf{J}^T\mathbf{W}^2\mathbf{J}\delta\mathbf{m} = \mathbf{J}^T\mathbf{W}^2\delta\mathbf{d}. \tag{2}$$

Here, the matrix $\mathbf{J}$ is the parameter sensitivity matrix or Jacobian, $\mathbf{W}$ is a weighting matrix to be specified further below, and $\delta\mathbf{m}$ is the change of the model vector $\mathbf{m}$ and quantifies the model update during a Marquardt iteration. The data misfit is given by the vector $\delta\mathbf{d}$ and is calculated from the differences between the observed data points d_i and the corresponding data predictions $p_i = f_i(\mathbf{m})$, where $i = 1, ..., N$. An appropriate forward modeling algorithm provides the function f for the data predictions.

An element J_{ij} of the Jacobian represents the partial derivative of the predicted datum p_i with respect to the model component m_j,

$$J_{ij} = \frac{\partial p_i}{\partial m_j}, \qquad i = 1, ..., N; \quad j = 1, ..., M. \tag{3}$$

The size of $\mathbf{J}$ is $N \times M$, given by the number of observed data points and the number of model unknowns, respectively. The calculation of the sensitivity matrix is usually the most time–consuming part of an inversion procedure, because this requires calculating the variation in the data produced by a change in the model parameters at each iteration. If sensitivities are associated with the resistivities of cells of finite volume, elegant ways based on the adjoint equation method can be used to calculate the Jacobian efficiently (@warning Citation ‘mcgi94’ on page 22 undefined; H¨ordt 1998). These methods employ the reciprocity relationship, and thus the computational effort is governed by the number of receiver stations for the inverted data rather than the number of unknowns. However, our approach involves floating layer thicknesses as parameters and only a few unknowns. Therefore, we use a perturbation method to obtain differential sensitivities. The small number of model parameters also makes this method computationally competitive. It is accomplished by perturbing each model parameter separately by a finite quantity. The responses of both the perturbed and unperturbed model are then used to compute the differences in eq. (3), yielding one column of the Jacobian for each perturbation. The expensive calculation of the Jacobian can be highly accelerated if a parallel computing platform is used. Because the forward simulations, needed for the perturbed model parameters, are carried out independently from each other, they can be distributed among several processors.

Following Jupp & Vozoff (1975), we solve eq. (2) by first calculating a Singular Value Decomposition (SVD) (Golub & Reinsch 1970) of $\mathbf{WJ}$,

$$\mathbf{WJ} = \mathbf{USV}^T, \tag{4}$$

where $\mathbf{U}$ is $M \times N$ and both $\mathbf{S}$ and $\mathbf{V}$ are $N \times N$. Here, $\mathbf{U}^T\mathbf{U} = \mathbf{I}_{M\times M}$, $\mathbf{V}^T\mathbf{V} = \mathbf{I}_{N\times N}$, and $\mathbf{S} = \mathrm{diag}(s_1, \ldots, s_N)$, where the singular values s_i are related to the eigenvalues of $\mathbf{J^T W^2 J}$. The SVD changes eq. (2) to

$$\delta\mathbf{m} = \mathbf{VS}^{-1}\mathbf{U}^T\mathbf{W}\delta\mathbf{d}. \tag{5}$$

To avoid problems when $\mathbf{S}$ is singular, $\mathbf{S}^{-1}$ is typically replaced by a diagonal matrix $\mathbf{S}^* = \mathrm{diag}(s_1^*, \ldots, s_N^*)$ with

$$\begin{aligned} s_i^* &= 1/s_i \quad \wedge \quad s_i \neq 0 \\ s_i^* &= 0 \quad \wedge \quad s_i = 0 \end{aligned} \tag{6}$$

In most geophysical inverse problems, however, $\mathbf{S}$ is not truly singular but ill conditioned, i.e. the smallest s_i is several orders of magnitude smaller than the largest eigenvalue. The entries of $\mathbf{S}^*$ can thus vary extremely, causing to overshoot the valid range of $\delta\mathbf{m}$, dictated by the Gauss-Newton scheme. Therefore, we employ a damped inversion approach (Vozoff & Jupp 1975) with the matrix $\mathbf{T}^{(P)} = \mathrm{diag}(t_1, \ldots, t_N)$, where

$$t_i^{(P)} = \frac{s_i^{2P-1}}{s_i^{2P} + \nu^{2P}}. \tag{7}$$

For $P \to \infty$, this yields a truncation inversion scheme. In our scheme, we choose $P = 2$, and eq. (5) becomes

$$\delta\mathbf{m} = \mathbf{V}\mathbf{S}^*\mathbf{T}^{(2)}\mathbf{U}^T\mathbf{W}\delta\mathbf{d}. \tag{8}$$

The parameter ν in eq. (7) controls the damping of the solution. In practice, the algorithm starts with $\nu = 0.1 \cdot \max(s_1, \ldots, s_N)$. If no misfit decrease is achieved, other updates are calculated by both multiplying and dividing ν by 2. This process can be accelerated by distributing multiple successive trial steps, each represented by a different ν, on a parallel computer. The first ν yielding a sufficient misfit improvement is chosen. Typically, ν decreases with later iterations.

Jupp & Vozoff (1975) derived in detail how the uncertainties of an inversion can be estimated by an analysis of $\mathbf{V}$, $\mathbf{T}^{(P)}$ and $\mathbf{U}$. Following their findings, we employ the so-called "importance" calculated from $\mathbf{V}$ and $\mathbf{T}^{(P)}$, to estimate a parameter's degree of resolution. This quantity has a range of 0–1, where 1 denotes maximum resolution. Another quantity calculated from the SVD, given by the "parameter error bounds", is in principle dependent on an assumed mean relative-error level. We choose a 10 % error level, according to the mean relative error of our data. Subject to this assumption, models within the error bounds will be considered equivalent to the solution.

Appendix B: Data and model parameter transformation

An important constraint on most model parameters, such as conductivity or layer thickness, is that they must be positive quantities. To enforce this constraint on the inverse solution, we follow the common practice of using a logarithmic transformation for the parameters m_j,

$$G(m_j) = \ln m_j, \tag{9}$$

which also has the advantage of stabilizing the solution if any parameter becomes very small or large.

Consequently, to achieve a preferably linear behaviour of the forward modelling function f on changes in the transformed parameters, one wants to apply appropriate data transformations. This also has the advantage of reducing the dynamic range of the data, to equalize the influence of each datum. LOTEM fields have widely different amplitudes at different times and receiver locations. Moreover, TEM measurements over multi-dimensional structures often involve sign reversals over the measurement time range, thus requiring that we distinguish between positive and negative data. Different possibilities exist to take both large amplitude variations and different signs into account. For example, transforming synthetic TEM data, Wang et al. (1994) use stitched logarithms with a linear range for small amplitudes within a predefined threshold. We consider a transformation scheme based upon the Area–Sinus–Hyperbolicus function, which has proven to be suitable for the 1D inversion of LOTEM data containing sign reversals. Such may appear when measuring for example horizontal magnetic induction time derivatives over a 1D Earth. Specifically, the transformation is given by

$$F(d_i, S) = \mathrm{a}rsinh\left(\frac{d_i}{S}\right) = \ln\left(\frac{d_i}{S} + \sqrt{\left(\frac{d_i}{S}\right)^2 + 1}\right). \tag{10}$$

Similar to the scheme of Wang et al. (1994), the function has a logarithmic behavior for arguments $\gg 1$ or $\ll -1$ and a linear one for arguments close to zero, where the scale factor S controls the changeover between both types. For example, decreasing S narrows the area around zero, where F is like a linear function; hence, this would be more similar to a logarithmic transformation, yet with the sign of the data retained. Over stitched logarithms, this scheme has the advantage that one does not need to specify a threshold for the linear range of the data. Usage of this type of

transformation is also justified by the exponential–like behavior of the model function, producing the predicted data. Experimenting with untransformed data produced poorer convergences for the shown inversion results.

Since we jointly invert multiple data sets (transients), it is desirable to keep the transformation similar for the different data sets. Therefore, we choose

$$S = \left| \frac{d_{max}}{10(\log d_{max} - \log d_{min})} \right|,$$

where d_{max} and d_{min} are the absolute values of the largest and the smallest datum in a data set. This way, the threshold is defined to be the maximum amplitude divided by a term representing the dynamic range of one transient.

Both data and model parameter transformations F and G carry over to the calculation of the Jacobian in eq. (3). A general rule is thus given by

$$J_{ij} = \frac{\partial p_i}{\partial m_j} \cdot \left(\frac{\partial G(m_j)}{\partial m_j} \right)^{-1} \cdot \frac{\partial F(p_i)}{\partial p_i}. \tag{11}$$

Using the transformations from eqs. (9) and (10), eq. (11) modifies to

$$J_{ij} = \frac{\partial p_i}{\partial m_j} m_j (S^2 + p_i^2)^{-\frac{1}{2}}. \tag{12}$$

Eq. (12) shows that a logarithmic function G involves scaling the corresponding column of $\mathbf{J}$ by the value m_j.

The data transformation F also requires transforming the data errors and thus the weighting matrix $\mathbf{W}$. Usually, $\mathbf{W}$ is a diagonal matrix, in which its entries w_{ii} are the reciprocal values of the standard deviations σ_i of the measurements (Jackson 1972). We assume that the uncertainties result from a zero-mean, Gaussian process that is independent in each of the observations. Then, the weighted misfit error

$$\epsilon = \sum_{i=1}^{N} (d_i - p_i)^2 w_{ii}^2 \tag{13}$$

is well known to be distributed as χ^2. Transforming a datum thus involves Gaussian propagation of the error, and the calculation of $\mathbf{W}$ changes to

$$w_{ii} = \left(\sigma_i \frac{\partial F(p_i)}{\partial p_i} \right)^{-1}.$$

Using these transformed weights, we assess the goodness of fit of the model predictions p_i to the measurements with the usual weighted least-squares criterion,

$$\chi^* = \sqrt{\frac{\epsilon}{N}}. \tag{14}$$

Appendix C: The VIBROTEM method

A few transients shown in Fig. 8 were generated using a source signal type that is different to the step signal, the one usually employed in the LOTEM method. The different signal waveforms were generated by the so-called VIBROTEM method. In this section, the basic principles of this method are outlined. For a more detailed treatment, the reader is referred to the works of Helwig et al. (1999), Helwig (2000), and references therein.

For the LOTEM method, the signal injected through the horizontal electric transmitter dipole typically has a switch-on or switch-off step form. The step generates a power spectrum that is proportional to $\frac{1}{f^2}$, where f is the frequency. Thus, most of the signal's energy is contained in low-frequencies, which makes the step signal favorable for large exploration depths. However, this frequency distribution is not always desired. One might be interested in shallower regions and thus it is preferable to have most of the signal's energy contained in higher frequencies. Also, in the presence of high noise, as we have experienced on Merapi's lower southern flank, the late-time portion of a transient can be distorted to such a degree that its data points have to be discarded or down-weighted in order to avoid a wrong or biased inversion result. In this case, it is desirable to shift the transmitter signal's frequency distribution towards a more intermediate frequency range. Thus, by giving up the late-time information of a transient, one seeks to improve the signal-to-noise ratio at earlier times, before the transient decay drops below the noise level.

Attenuating low-frequency bands of the source signal can be achieved by using so-called pseudo-random-binary-sequences (PRBS) as waveforms. Instead of a step signal, this technique injects a continuous signal sequence into the ground. The PRBS sequences have a triangular-shaped and impulse-like autocorrelation function. Similar to the VIBROSEIS method, the recorded time series are cross-correlated with the transmitted waveform to generate the transient response. It follows that VIBROTEM transients are effectively the time derivative of a step response.

Fig. 11 shows a comparison between the transients generated by the LOTEM and VIBROTEM methods. The vertical magnetic field data were measured at Station 40–bz, where anthropogenic noise due to nearby settlements was exceptionally high. To compare the two data sets, the VIBROTEM transient has been integrated with respect to time, in order to produce a step response. Note that both transients show a strong distortion by noise at the times after 20 ms. We discarded these data points from the inversion data set. The LOTEM transient shows noise effects beginning before 10 ms, while the PRBS signal is of much better quality at these times. The improvement in signal-to-noise ratio is approximately a factor of five.

One notes a discrepancy of the two curves at the earliest times, which is caused by the deviation of the PRBS sequence's autocorrelation function from an impulse. During the inversion, this effect is taken into account by convolution of the simulated data of each station with its corresponding autocorrelation function.

REFERENCES

Archie, G. E., 1942. The electrical resistivity log as an aid in determining some reservoir characteristics, Tran. AIME, **146**, 54–67.

Aubert, M., Dana, I. & Gourgaud, A., 2000. Internal structure of the Merapi summit from self–potential measurements, J. Volc. Geother. Res., **100**, 337–343.

Beauducel, F. & Cornet, F. H., 1999. Collection and three-dimensional modeling of GPS and tilt data at Merapi Volcano, Java, J. Geophys. Res., **104**, 725–736.

Camus, G., Gourgaud, A. & Mossand-Berthommier, P.-C., 2000. Merapi (Central Java, Indonesia): An outline of the structural and magmatological evolution, with a special emphasis to the major pyroclastic events, J. Volc. Geother. Res., **100**, 139–163.

Commer, M., Helwig, S. L., H¨ordt, A. & Tezkan, B., 2005. Interpretation of long-offset TEM data from Mount Merapi (Indonesia) using a 3D optimization approach, J. Geophys. Res., **110**, No. B3, B0320710.1029/2004JB003206.

Commer, M., 2003. Three–dimensional inversion of transient electromagnetic data: A comparative study, PhD thesis, University of Cologne, Cologne.

Druskin, V. L. & Knizhnerman, L. A., 1988. A spectral semi-discrete method for the numerical solution of 3D-nonstationary problems in electrical prospecting, Physics of the solid Earth, **24**, 641–648.

Druskin, V. & Knizhnerman, L., 1994. Spectral approach to solving three-dimensional maxwell's diffusion equations in the time and frequency domains, Radio Science, **29**, 937–953.

Fitterman, D. V., Stanley, W. D. & Bisdorf, R. J., 1988. Electrical structure of Newberry Volcano, Oregon, J. Geophys. Res., **93**, 10119–10134.

Fl´ovenz, O., Georgsson, L. S. &Árnason, K., 1985. Resistivity structure of the upper crust in Iceland, J. Geophys. Res., **90**, 10136–10150.

Friedel, S., Brunner, I., Jacobs, F. & R¨ucker, C., 2000. New results from DC resistivity imaging along the flanks of Merapi Volcano, in *Decade-Volcanoes under Investigation*, Vol. IV/2000, pp. 23–29, ed. Zschau, J. & Westerhaus, M., DGG, Hannover.

Gauthier, P. J. & Condomines, M., 1999. 210P–226Ra radioactive disequilibria in recent lavas and radon degassing: inferences on the magma chamber dynamics at Stromboli and Merapi volcanoes, Earth Planet. Sci. Lett., **172**, 111–126.

Gerstenecker, C., L¨aufer, G., Snitil, B. & Wrobel, B., 1998. Digital elevation models for Mount Merapi, in *Decade-Volcanoes under Investigation*, Vol. III/1998, pp. 65–68, ed. Zschau, J. & Westerhaus, M., DGG, Hannover.

Gertisser, R., 2001. Gunung Merapi (Java, Indonesien): Eruptionsgeschichte und magmatische Evolution eines Hochrisiko–Vulkans, PhD thesis, Universit¨at Freiburg.

Gertisser, R. & Keller, J., 2003. Trace element and Sr, Nd, Pb and O isotope variations in medium-K and high-K volcanic rocks from Merapi Volcano, Central Java, Indonesia: evidence for the involvement of subducted sediments in Sunda arc magma genesis, J. Petrol., **44**, 457–489.

Golub, G. H. & Reinsch, C., 1970. Singular value decomposition and least–squares solutions, Num. Math., **14**, 403–420.

Hanstein, T., 1996. Digitale Optimalfilter f¨ur LOTEM Daten, in *Protokollüber das 16. Kolloquium Elektromagnetische Tiefenforschung*, pp. 320–328, ed. Bahr, K. & Junge, A., DGG, Potsdam.

Helwig, S., H¨ordt, A. & Hanstein, T., 1999. The VIBROTEM method, in *69th Annual International Meeting, SEG, Expanded Abstracts*, pp. 283-285, Houston, Texas.

Helwig, S. L., 2000. VIBROTEM, PhD thesis, University of Cologne, Cologne.

H¨ordt, A. & M¨uller, M., 2000. Understanding LOTEM data from mountainous terrain, Geophysics, **65**, 1113–1123.

H¨ordt, A. & Scholl, C., 2004. The effect of local distortions on time–domain electromagnetic measurements, Geophysics, **69**, 87–96.

H¨ordt, A., 1998. Calculation of electromagnetic sensitivities in the time domain, Geophys. J. Int., **133**, 713–720.

Huang, H. & Palacky, G. J., 1991. Damped least–squares inversion of time–domain airborne EM data based on singular value decomposition, Geophys. Prospect., **39**, 827–844.

Jackson, D. B. & Keller, G. V., 1972. An electromagnetic sounding survey of the summit of Kilauea Volcano, Hawaii, J. Geophys. Res., **77**, 4957–4965.

Jackson, D. D., 1972. Interpretation of inaccurate, insufficient and inconsistent data, Geophys. J. R. astr. Soc., **28**, 97–109.

Jupp, D. L. B. & Vozoff, K., 1975. Stable iterative methods for the inversion of geophysical data, Geophys. J. R. astr. Soc., **42**, 957–976.

Kalscheuer, T., Helwig, S. L., Tezkan, B. & Commer, M., 2004. Multidimensional modelling of LOTEM data collected at the south flank of Mt. Merapi, Indonesia, in *Protokoll über das 20. Kolloquium Elektromagnetische Tiefenforschung*, pp. 104–113, ed. Hördt, A. & Stoll, J., DGG, Potsdam.

Keller, G. V., 1988. Rock and mineral properties, in *Electromagnetic Methods in Applied Geophysics*, pp. 13–51, ed. Nabighian, M. N., SED, Tulsa, Oklahoma.

Lenat, J. F., Fitterman, D. V., Jackson, D. B. & Labazuy, P., 2001. Geoelectrical structure of the central zone of Piton de la Fournaise Volcano (Réunion), Bulletin of Volcanology, **62**, 75–89.

Levenberg, K., 1944. A method for the solution of certain nonlinear problems in least squares, Quarterly of Applied Mathematics, **2**, 164–168.

Marquardt, D. W., 1963. An algorithm for least-squares estimation of non-linear parameters, SIAM J., **11**, 431–441.

Moskow, S., Druskin, V., Habashy, T., Lee, P. & Davydychewa, S., 1999. A finite difference scheme for elliptic equations with rough coefficients using a cartesian grid nonconforming to interfaces, SIAM J. Numerical Analysis, **36**, 442–464.

Müller, A. & Haak, V., 2004. 3-D modeling of the deep electrical conductivity of Merapi Volcano (Central Java): integrating magnetotellurics, induction vectors and the effects of steep topography, J. Volc. Geother. Res., **138**, 205–222.

Müller, M., Hördt, A. & Neubauer, F. M., 2002. Internal structure of Mount Merapi, Indonesia, derived from long–offset transient electromagnetic data, J. Geophys. Res., **107**, ECV 2–1–ECV 2–14.

Natori, H., 1978. Cenozoic sequence in Jawa and adjacent areas, in *Gravity and geologic studies in Jawa, Indonesia*, pp. 76–81, ed. Untung, M. & Sato, Y., Geological Survey of Indonesia and Geological Survey of Japan, Bandung.

Nesbitt, B. E., 1993. Electrical resistivities of crustal fluids, J. Geophys. Res., **98**, 4301–4310.

Newhall, C. G., Bronto, S., Alloway, B., Banks, N. G., Bahar, I. & Marmol, M. A. D., 2000. 10000 years of explosive eruptions of Merapi Volcano, Central Java: archaeological and modern implications, J. Volc. Geother. Res., **100**, 9–50.

Newman, G. A., 1989. Deep transient electromagnetic soundings with a grounded source over near-surface conductors, Geophys. J., **98**, 587–601.

Ratdomopurbo, A. & Poupinet, G., 1995. Monitoring a temporal change of seismic velocity in a volcano: application to the 1992 eruption of Mt. Merapi (Indonesia), Geophys. Res. Lett., **22**, 775–778.

Ritter, O., Hoffmann-Rothe, A., Müller, A., Dwipa, S., Arsadi, E. M., Mahfi, A., Nurnusanto, I., Byrdina,

S., Echternacht, F. & Haak, V., 1998. A magnetotelluric profile across Central Java, Indonesia, Geophys. Res. Lett., **25**, 4265–4268.

R¨uter, H. & Strack, K.-M., 1991. Bedrock exploration system using transient electromagnetic measurements, Patent PCT/DE91/00238.

Siswowidjoyo, S., Suryo, I. & Yokoyama, I., 1995. Magma eruption rates of Merapi Volcano, Central Java, Indonesia, during one century (1890–1992), Bull. Volcanol., **57**, 111–116.

Strack, K. M., 1992. *Exploration with Deep Transient Electromagnetics*, Elsevier, Amsterdam.

Tiede, C., Camacho, A. G., Gerstenecker, C., Fern´andez, J. & Suyanto, I., 2005. Modeling the density at Merapi volcano area, Indonesia, via the inverse gravimetric problem, Geochem. Geophys. Geosys. G3, **6**, doi:10.1029/2005GC000986.

Ussher, G., Harvey, C., Johnstone, R. & Anderson, E., 2000. Understanding the resistivities observed in geothermal systems, *Proc. World Geoth. Congr., Kyushu-Tohoku, Japan*, 1915–1920.

Van Bemmelen, R. W., 1949. *The geology of Indonesia*, Vol. IA, Government Printing Office, The Hague.

Vozoff, K. & Jupp, D. L. B., 1975. Joint Inversion of Geophysical Data, Geophys. J. R. astr. Soc., **42**, 977–991.

Wang, T., Oristaglio, M., Tripp, A. & Hohmann, G., 1994. Inversion of diffusive transient elctromagnetic data by a conjugate–gradient method, Radio Science, **29**, 1143–1156.

Wassermann, J., Ohrnberger, M., Scherbaum, F., 1998. Continuous measurements at Merapi Volcano (Java, Indonesia) using a network of small–scale seismograph arrays, in *Decade-Volcanoes under Investigation*, Vol. III/1998, pp. 81–82, ed. Zschau, J. & Westerhaus, M., DGG, Potsam.

Zimmer, M., Erzinger, J. & Sulistiyo, Y., 2000. Continuous chromatographic gas measurements on Merapi volcano, Indonesia, in *Decade-Volcanoes under Investigation*, Vol. IV/2000, pp. 87–91, ed. Buttkus, B., Greinwald, S. & Ostwald, J., DGG, Hannover.

Zschau, J., Sukhyar, R., Purbawinata, M. A., L¨uhr, B. & Westerhaus, M., 1998. Project MERAPI – Interdisciplinary Research at a High-Risk Volcano, in *Decade-Volcanoes under Investigation*, Vol. III/1998, pp. 3–8, ed. Zschau, J. & Westerhaus, M., DGG, Potsdam.

Table 1. Parameter quantities, error bounds and importances for inversion results A and B

Model A

	Parameter	Result	Error bounds	Importance
1	ϱ_1 ($\Omega \cdot$ m)	222.37	192.95–256.27	0.99
2	h_1 (m)	237.70	193.39–292.17	0.97
3	ϱ_2 ($\Omega \cdot$ m)	86.66	77.09–97.41	0.99
4	h_2 (m)	737.82	674.06–807.62	0.99
5	ϱ_3 ($\Omega \cdot$ m)	4.30	3.31–5.57	0.92
6	h_3 (m)	320.50	292.07–351.71	1.00
7	ϱ_4 ($\Omega \cdot$ m)	0.67	0.49–0.91	0.81

Model B

	Parameter	Result	Error bounds	Importance
1	ϱ_1 ($\Omega \cdot$ m)	256.57	238.60–275.89	0.92
2	h_1 (m)	218.97	203.21–235.95	0.90
3	ϱ_2 ($\Omega \cdot$ m)	67.93	63.87–72.24	0.96
4	h_2 (m)	803.49	782.16–825.41	0.99
5	ϱ_3 ($\Omega \cdot$ m)	0.13	0.13–0.14	0.24
6	ϱ_{block1} ($\Omega \cdot$ m)	819.26	752.25–892.24	0.75
7	ϱ_{block2} ($\Omega \cdot$ m)	66.97	62.88–71.32	0.43
8	ϱ_{block3} ($\Omega \cdot$ m)	8.55	7.84–9.33	0.89

Table 2. Salinity estimates for the layered background of Model A. Salinity estimates are derived from error bounds of bulk resistivities ϱ, fluid resistivities ϱ_w, and temperature T. The second estimates for Layer 4 are based on a different form of Archie's law.

Layer	ϱ ($\Omega \cdot$ m)	ϱ_w ($\Omega \cdot$ m)	T (°C)	Salinity (eq. wt. % NaCl)
1	193–256	1.9–10.2	20–44	0.005–0.2
2	77–97	0.8–3.9	44–118	0.06–0.7
3	3.3–5.6	0.033–0.224	118–150	0.7–8
4	0.5–0.9	0.005–0.036	150+	7–50+
4	0.5–0.9	0.02–0.09	150+	2–10

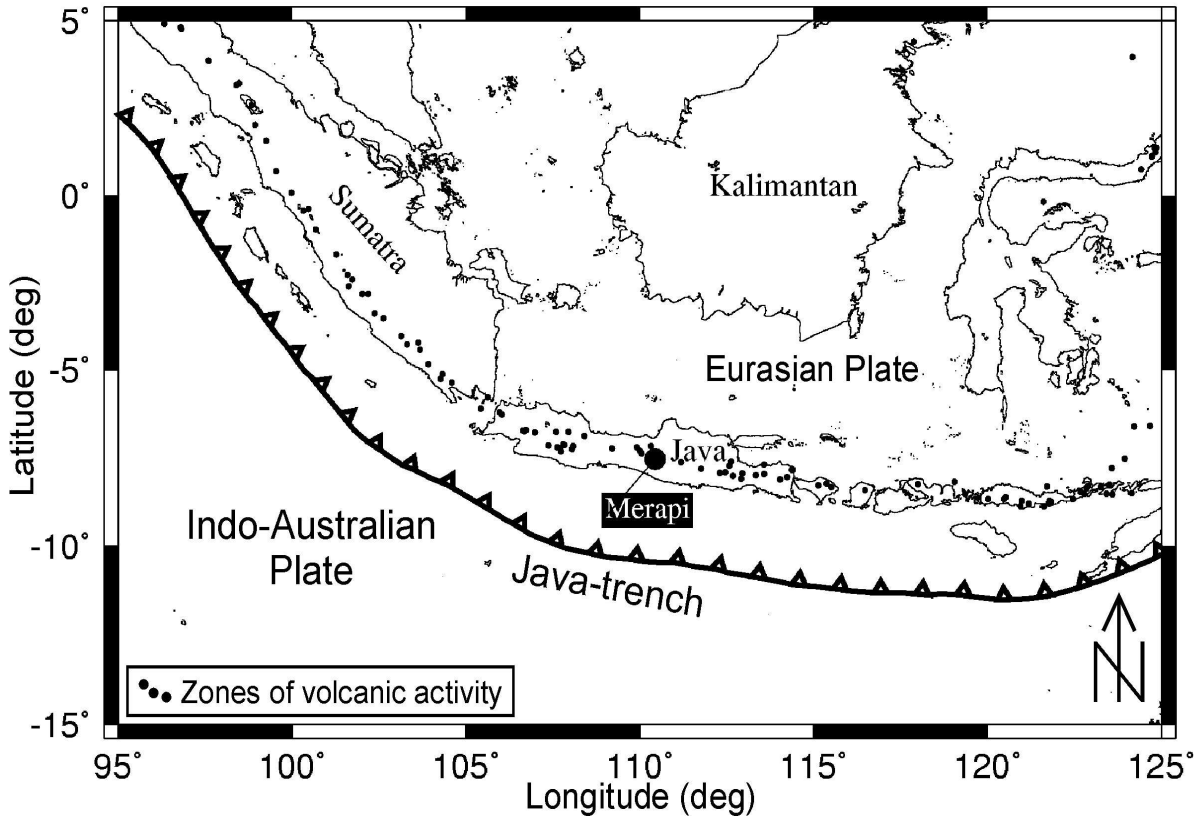

Figure 1. Indonesia and the location of Merapi Volcano.

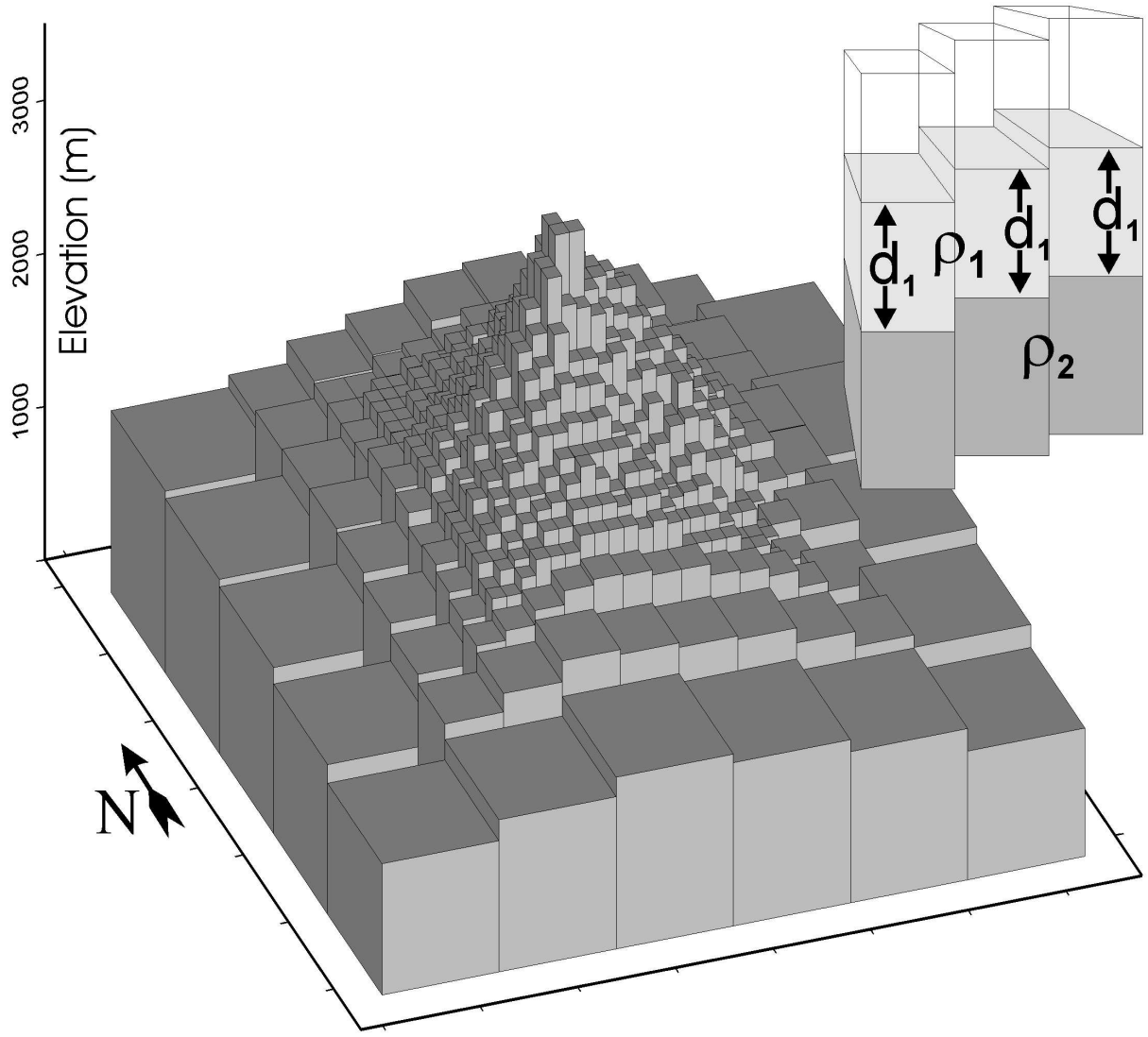

Figure 2. Modeling of the terrain structure with vertical columns. The figure in the upper right corner illustrates the design of two layers that follow the topography.

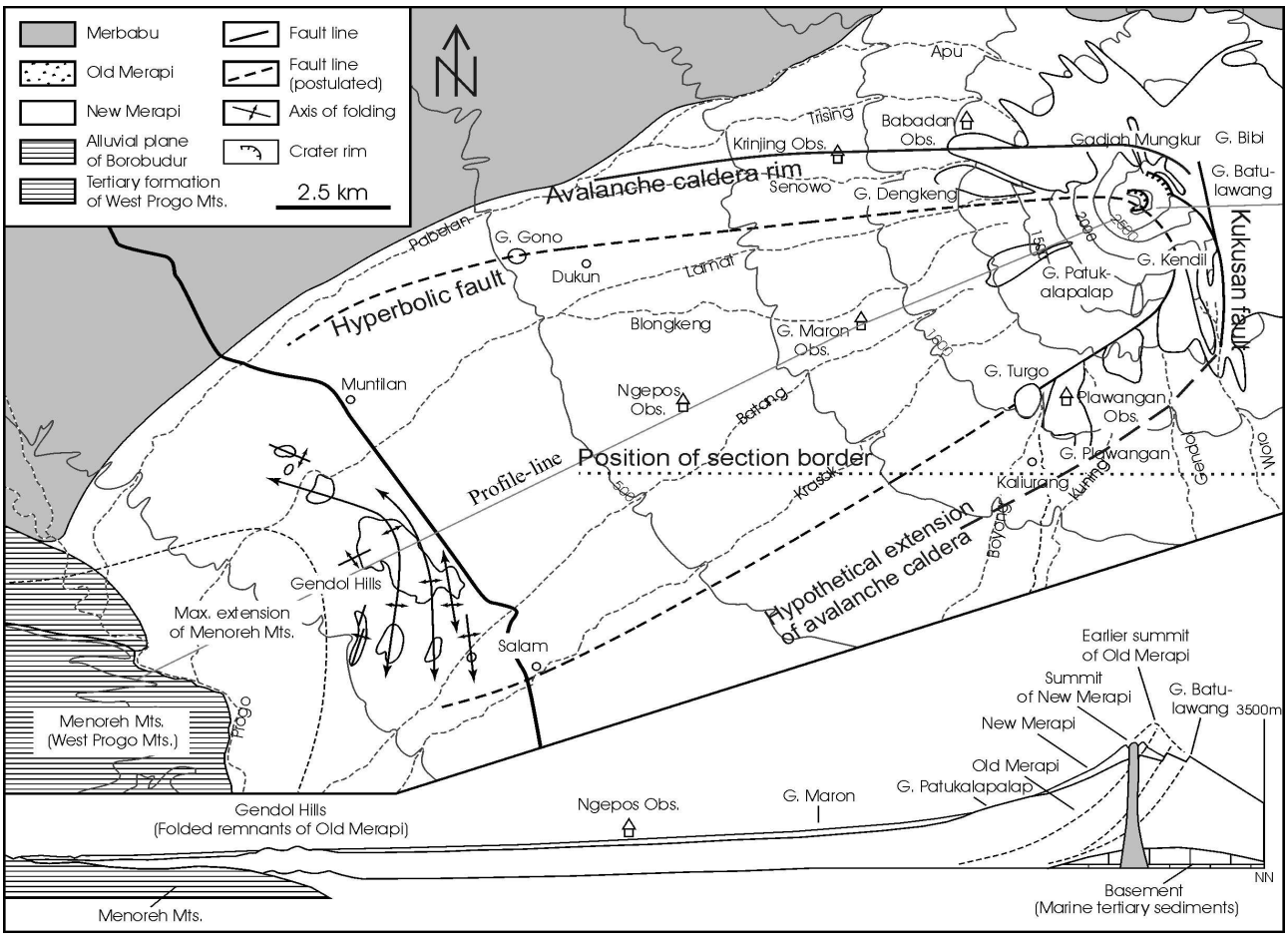

Figure 3. Geological sketch map of Merapi, after Gertisser (2001), based on Van Bemmelen (1949). The lower fi gure shows a section through the western sector of the volcano (profi le line). The horizontal dotted line at ≈ 7 km south of the summit shows the location of the section border in our model results.

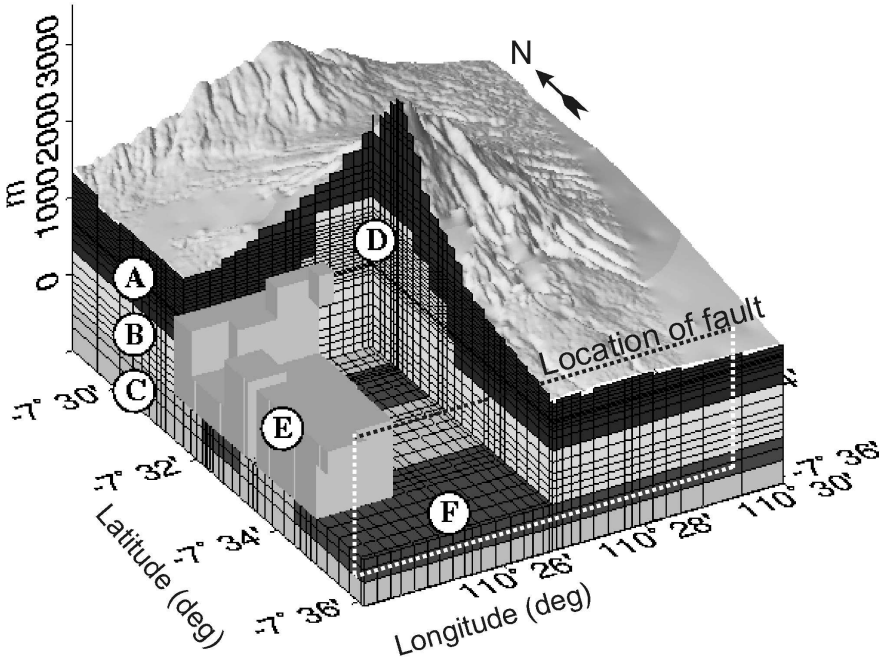

Figure 4. Vertical cross section through the summit from the 3D model derived from MT measurements (after M¨uller & Haak, 2004). Structures: (A) Upper layer (100 $\Omega \cdot$ m), (B) Intermediate conducting layer (10 $\Omega \cdot$ m), (C) Conducting layer (1 $\Omega \cdot$ m), (D) Central conductor (10 $\Omega \cdot$ m), (E) SW anomaly (1 $\Omega \cdot$ m), (F) Two extended conductors (0.1 $\Omega \cdot$ m). The dashed line indicates the location of the fault position assumed from earlier LOTEM studies.

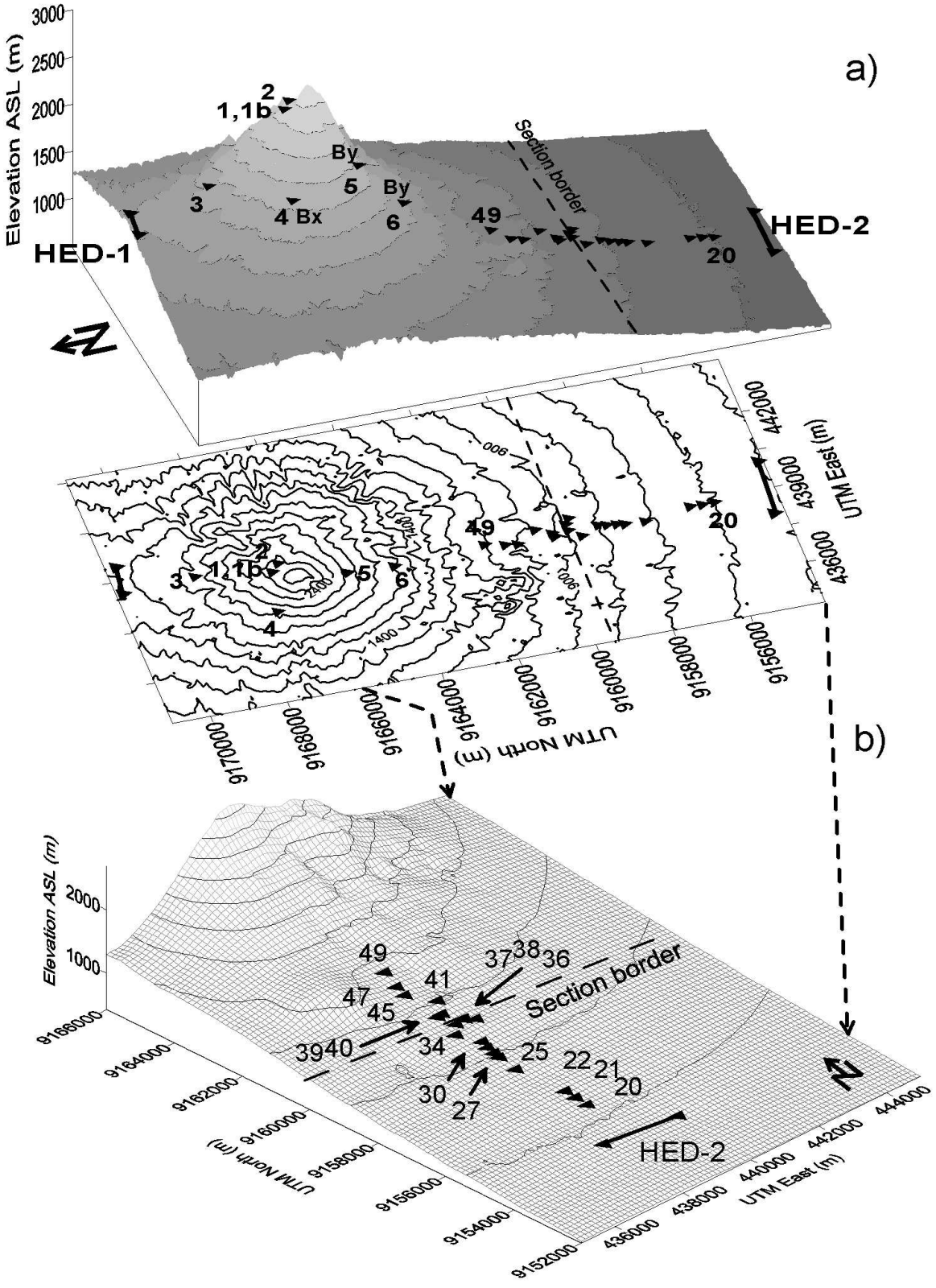

Figure 5. (a) Location of all inverted LOTEM stations and (b) southern flank profile. The dashed line indicates the plane which divides the model into two layered sections. Note that the stations are not numbered consecutively.

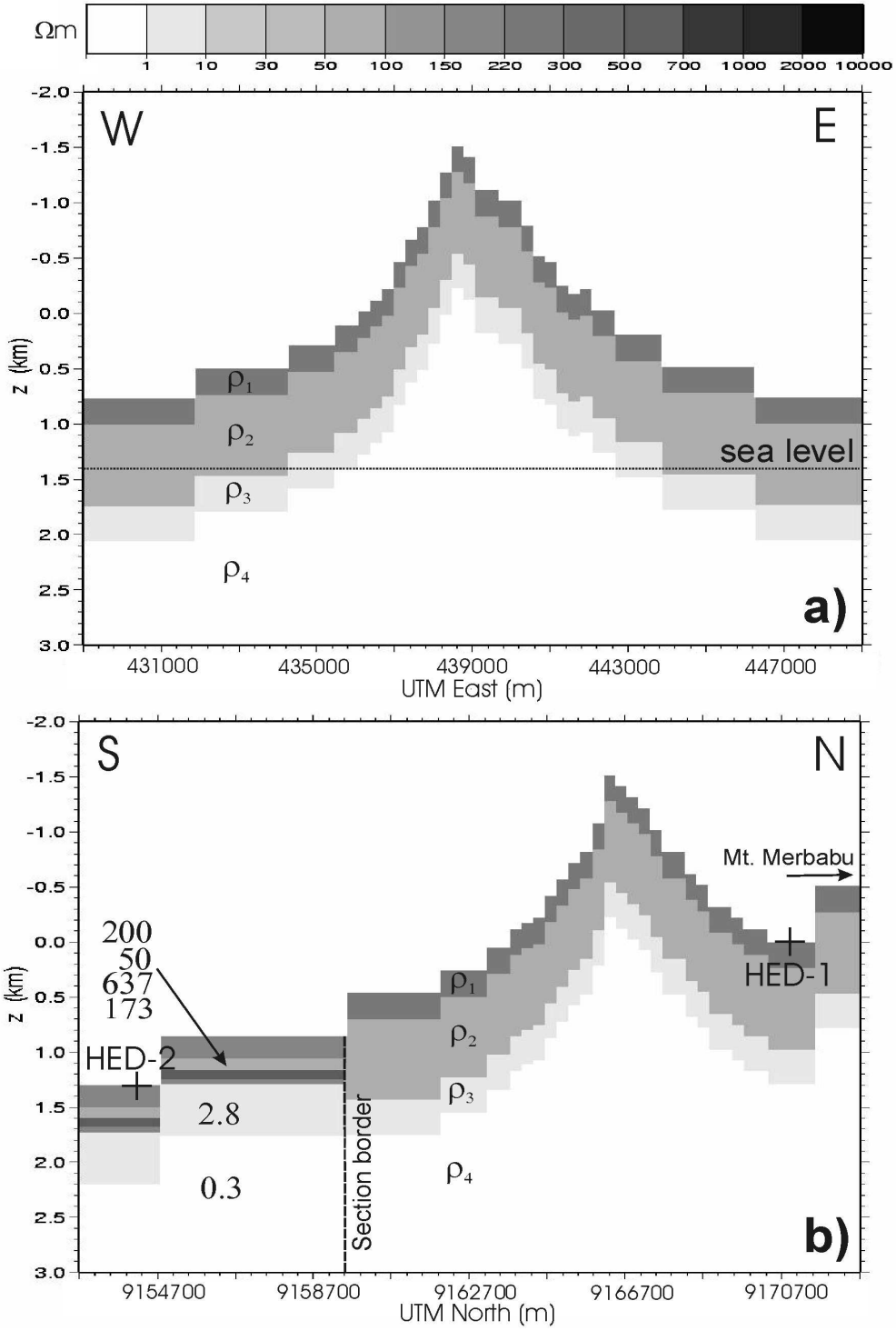

Figure 6. Inversion result for a layered model (Model A) shown in a west–east (upper) and south–north (lower) section through the summit. The six layer resistivities of the southern section are given in $\Omega \cdot \mathrm{m}$ in the lower fi gure. The fi nal parameter quantities are listed in Table 1.

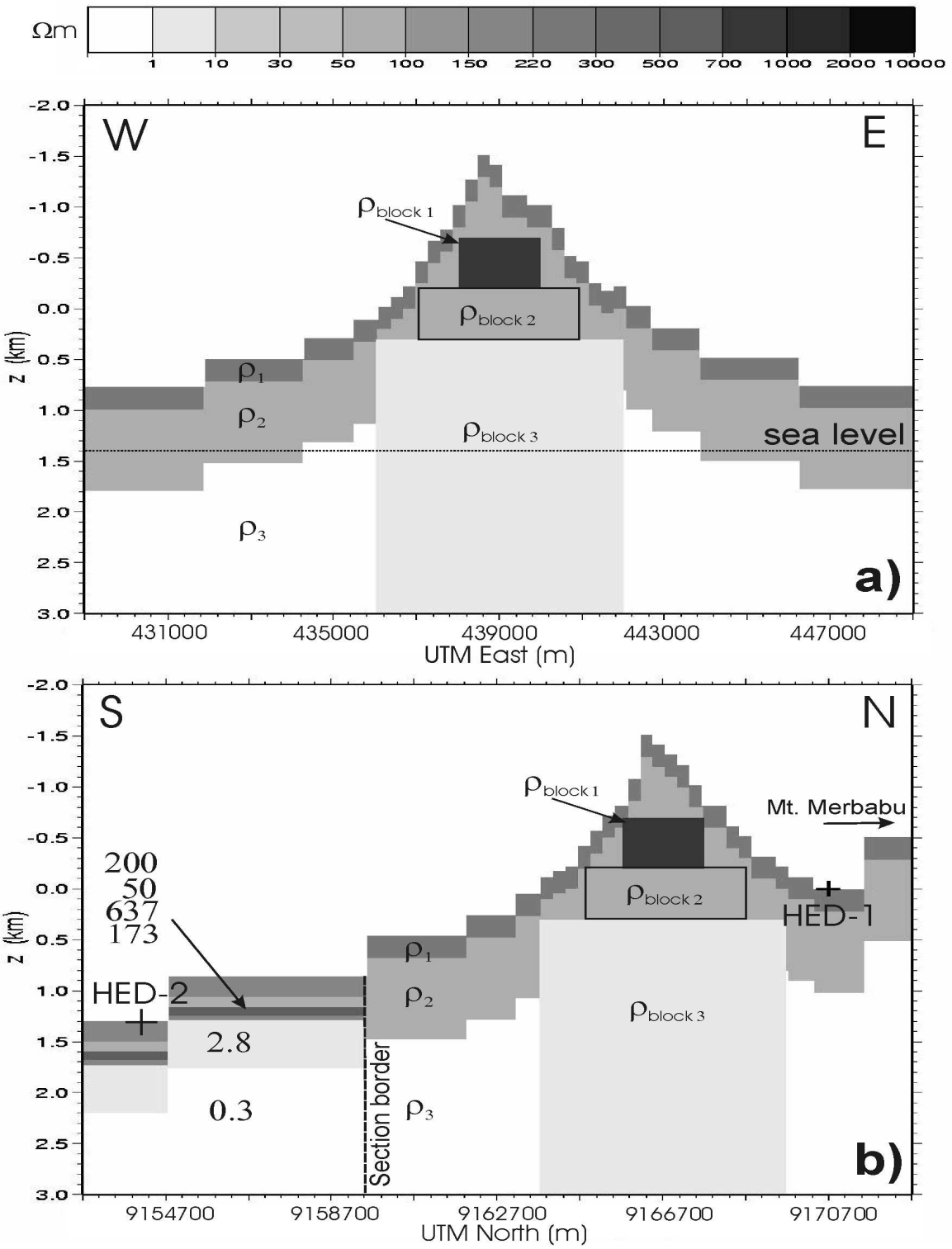

Figure 7. Sections of Model B through the summit. The parameter quantities are listed in Table 1. The parameterization comprises three layers and three 3D blocks.

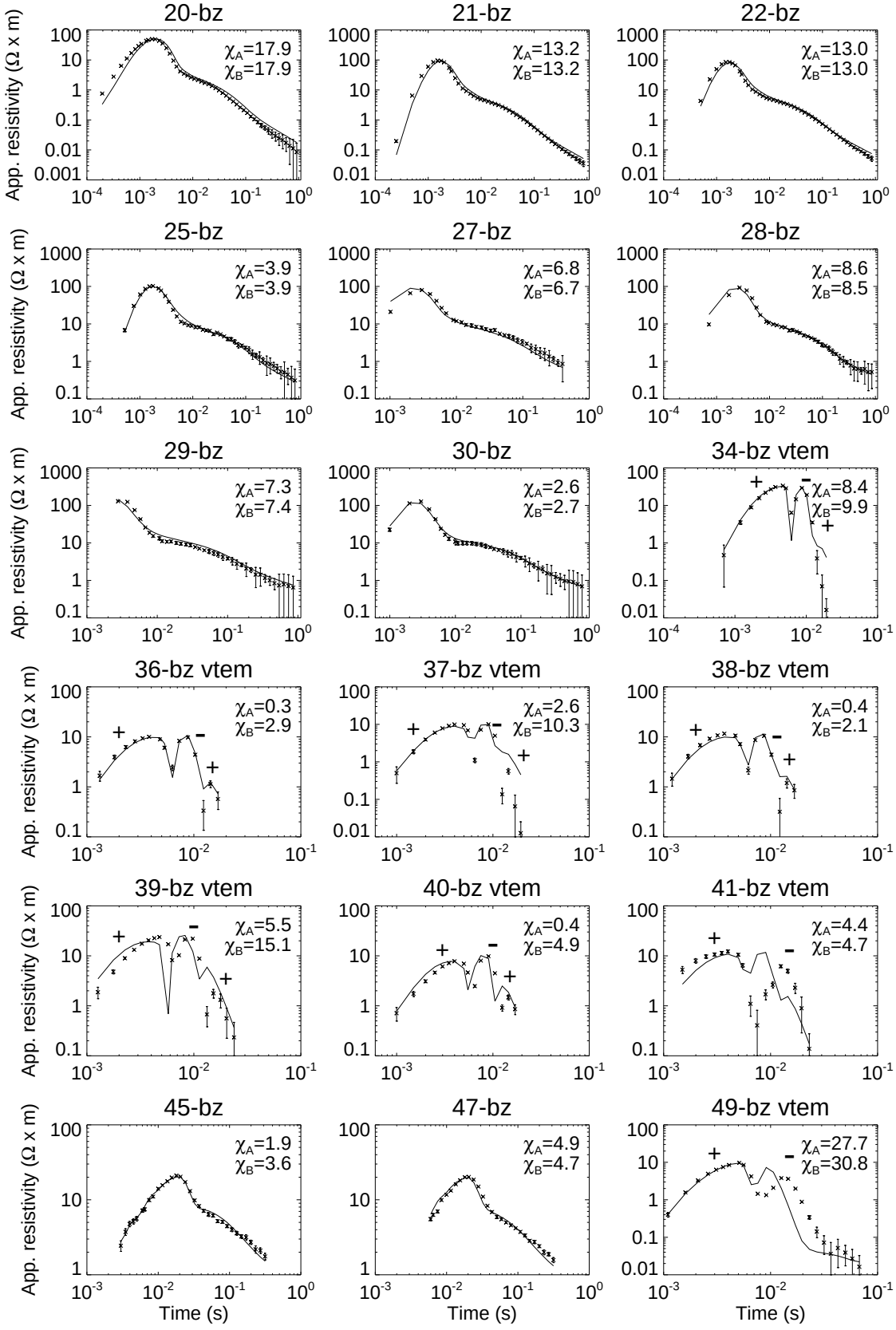
20-bz
χA=17.9
χB=17.9
21-bz
χA=13.2
χB=13.2
22-bz
χA=13.0
χB=13.0
25-bz
χA=3.9
χB=3.9
27-bz
χA=6.8
χB=6.7
28-bz
χA=8.6
χB=8.5
29-bz
χA=7.3
χB=7.4
30-bz
χA=2.6
χB=2.7
34-bz vtem
χA=8.4
χB=9.9
36-bz vtem
χA=0.3
χB=2.9
37-bz vtem
χA=2.6
χB=10.3
38-bz vtem
χA=0.4
χB=2.1
39-bz vtem
χA=5.5
χB=15.1
40-bz vtem
χA=0.4
χB=4.9
41-bz vtem
χA=4.4
χB=4.7
45-bz
χA=1.9
χB=3.6
47-bz
χA=4.9
χB=4.7
49-bz vtem
χA=27.7
χB=30.8
App. resistivity (Ω x m)
Time (s)

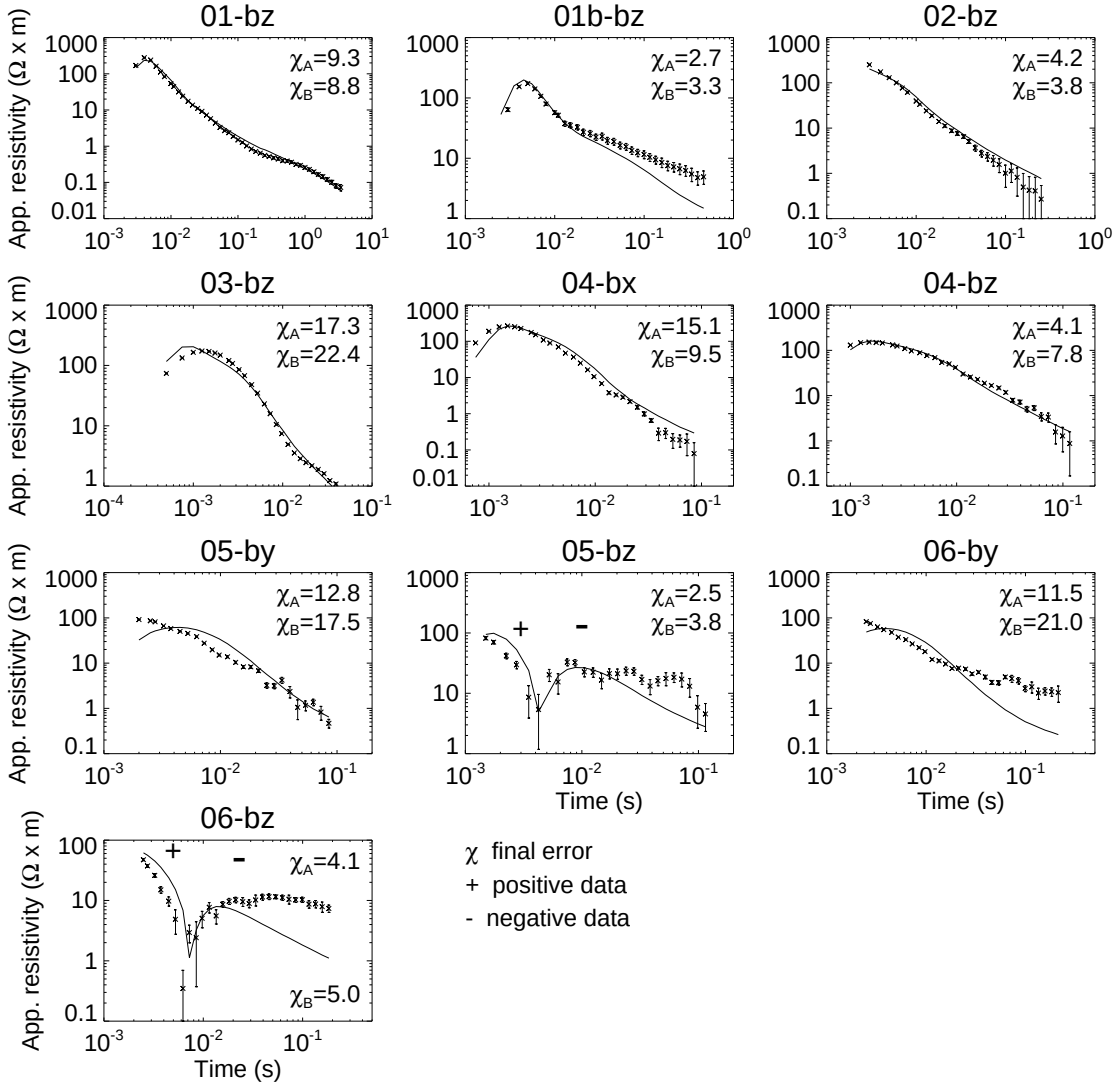

Figure 8. Data fit (solid lines) calculated from Model A (Fig. 6). The numbers above each data plot refer to the station numbers in Fig. 5. Stations 20-49 belong to the profile south from the summmit, stations 1-6 are located around the summit. Vertical fields are denoted by "bz" and horizontal fields by "bx" and "by". The corresponding misfit errors are χ_A for Model A, while χ_B are the errors calculated from Model B. VIBROTEM transients are denoted by "vtem".

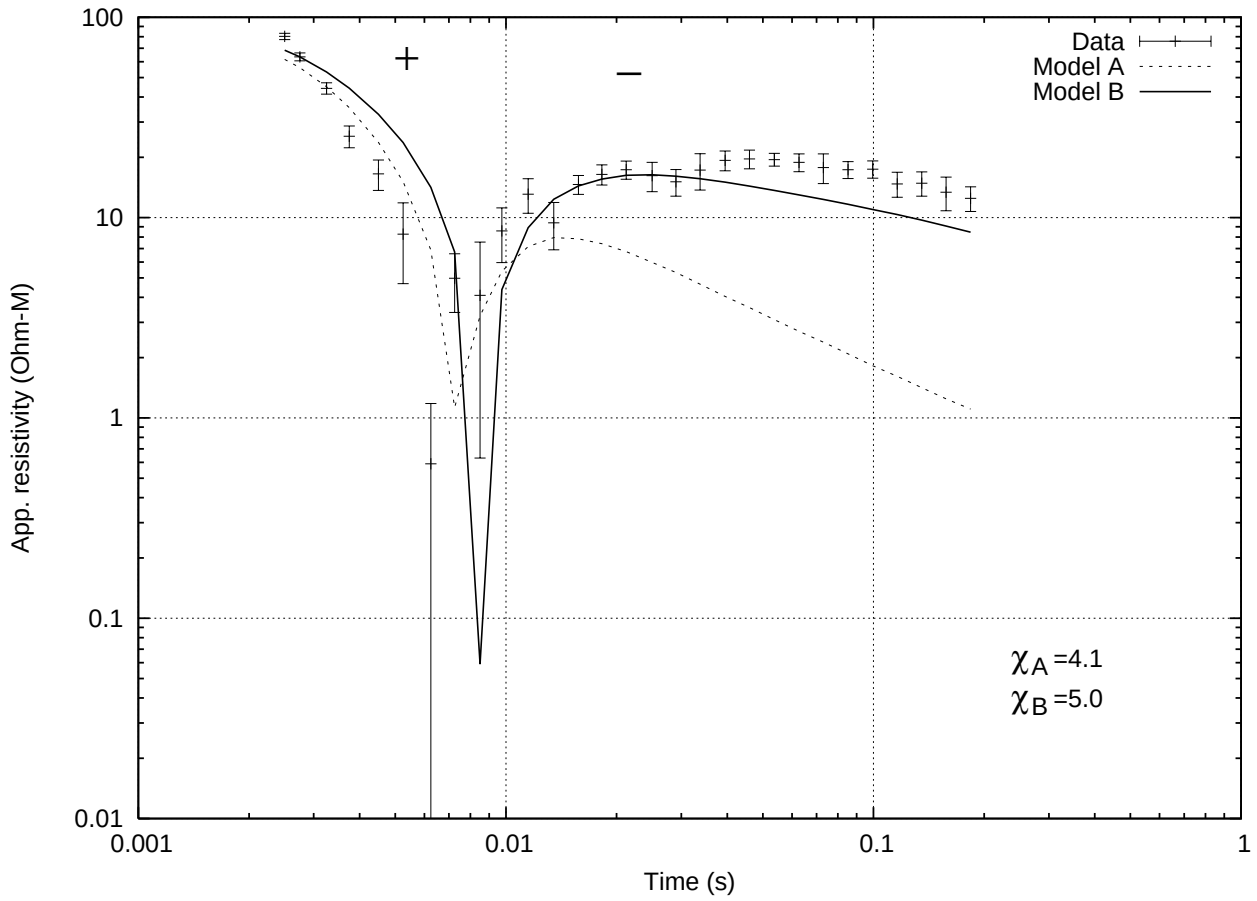

Figure 9. Comparison of the predicted data of Station 06–bz calculated from Model A (dashed line) and Model B (solid line).

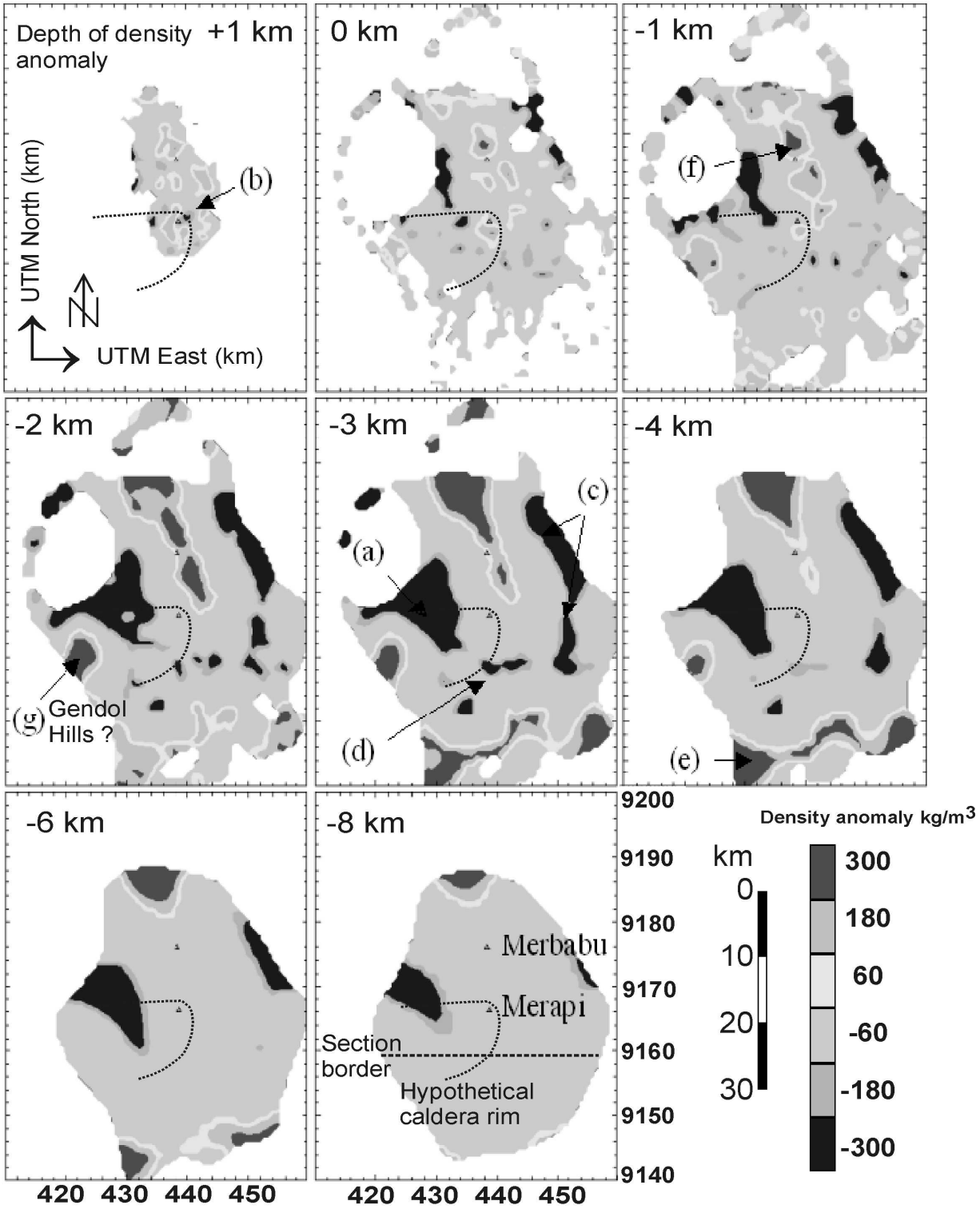

Figure 10. Anomalous density contrasts (Tiede et al., 2005) shown together with the hypothetical caldera and the proposed southward extension. Coordinates are based on UTM and the depths on the EGM96 geoid.

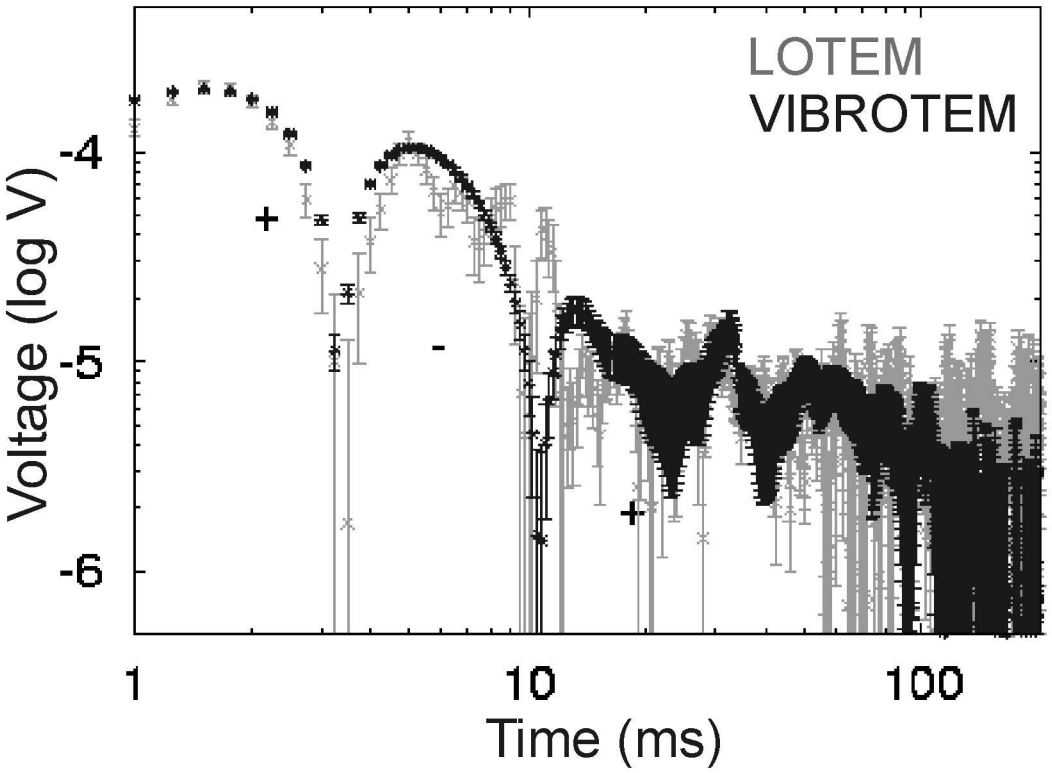

Figure 11. Vertical magnetic field transient at Station 40, measured with the LOTEM (gray) and VIBROTEM (black) methods. The VIBROTEM transient is less affected by high frequency noise. It has been time-integrated for this comparison.